Doctoral Dissertation

Theoretical Study of Geometry, Size and Alloying Effects on the Reactivity of Small Pt Clusters

(白金微小クラスタ反応性におけるクラスタ構造・サイズ・依存性及び合金化効果に関する理論的研究)

Ferensa Oemry

January 2014

Department of Applied Physics

Graduate School of Engineering

Osaka University

ABSTRACT

Catalytic reaction of small Pt clusters involving oxygen has been one of the most intensive research studies in Pt-based heterogeneous catalysts that play a vital role for the development of diesel oxidation catalyst (DOC). Moreover, there are still many major issues in DOC such as oxygen poisoning that has not been solved yet and this issue needs to be addressed properly. For that purpose, a rigorous study on bonding interaction between small Pt clusters and oxygen was conducted. The first part of this study discusses the role of geometry and support effects on Pt_4 isomers (tetrahedron and planar rhombus) where the work was initially motivated by mass spectrometer studies on gas-phase Pt clusters. The reactivity of these Pt_4 isomers was evaluated using NO molecule as testing adsorbate that being carried out in the conditions with and without the presence of γ-Al_2O_3 (111) surface as the support. The result shows that NO adsorption on tetrahedron-structured Pt_4 cluster is weaker as compared to the planar rhombus case in both conditions (isolated and with the support). Interestingly, the most preferable adsorption site for NO molecule in tetrahedron-structured Pt_4 cluster is support-dependent as validated by early molecular dynamics study. However, this rule does not apply for Pt_4 cluster with planar rhombus structure. Moreover, bonding stability between the cluster and its support is also geometry-dependent where tetrahedron-structured Pt_4 cluster is more stable on Al_2O_3 surface. The reason is that two of three Pt atoms in the cluster interact altogether with both Al and O atoms of Al_2O_3 surface where there is only one in planar rhombus case. These Pt-Al bonds could reduce repulsive contribution from Pt-O bonds by transferring some electrons from anti-bonding of O(2p)-Pt(5d) to bonding part of Al(3p)-Pt(5d).

The next study elaborates O_2 dissociative adsorption process on isolated Pt_4 and Pt_{10} clusters by taking into consideration the cluster reconstruction effect. Both clusters acquire similar geometric structure, tetrahedron, where Pt_{10} cluster is a bigger representative size of Pt_4 cluster. The concept of interstitial bonding orbital (IBO) is introduced to explain the mechanism that initially triggers geometry reconstruction in small Pt clusters, particularly Pt_{10}. In brief, when oxygen adsorbs on the clusters the IBO strength will be weakened and the clusters will undergo atom rearrangement that leads to structural deformation. Moreover, cluster that could undergo structural deformation (Pt_{10} cluster) is found to promote oxygen dissociation without having to experience any energy barrier. Based on

careful analysis, it shows that any considerable rise of energy barrier during O_2 dissociation could be avoided if the cluster can accommodate O–O bond elongation by rearranging their atoms in order to maintain the balance of intramolecular forces between their neighbor atoms. However, if Pt atoms in the cluster are hardly moving, they could inflict disproportionate intramolecular forces among the atoms and induce a rising energy (barrier) fluctuation during O_2 dissociation process. This result brings a profound implication that suggests oxygen that adsorbed on more easily-reconstructed Pt cluster is more likely to undergo dissociation with lesser or no energy barrier.

In the final work of this study, core-shell Ni@Pt cluster is proposed as a prospective catalyst candidate for DOC. In comparison to pure Pt cluster, core-shell Ni@Pt cluster is able to reduce Pt-O bonding strength. Furthermore, weaker oxygen adsorption energy that being observed in Ni@Pt cluster is mainly caused by compressive strain effect on surface Pt-Pt bonds due to bond distances mismatch at Pt/Ni interface. However, cluster reconstruction that occurs on Ni@Pt cluster could loosen the strained Pt-Pt bonds and increase oxygen adsorption energy. Similar result is also found in pure Pt cluster since the cluster's surface Pt-Pt bonds are also less rigid and their bond lengths can be easily deviated. The results also indicate that cluster reconstruction phenomenon during oxidation process is real and experimentally measurable. By comparing data from EXAFS measurement and DFT calculation, it was shown that the first nearest neighbor (1NN) Pt-Pt bond distribution profiles from two different data demonstrate a similar general trend where the amplitude of 1NN of surface Pt-Pt bonds would decrease as more oxygen absorbed on the clusters. In addition, three important roles of Ni atoms in core-shell Ni@Pt cluster are reducing Pt-O bonding strength, suppressing the effect of cluster reconstruction and, in particular case, preventing bond breaking process on surface Pt-Pt bonds. Lastly, the influence of oxygen-induced cluster reconstruction on the stability of bonding interaction at core/shell interface is investigated. The result shows that the bonding interaction of Pt(core)-Pt(shell) bonds in pure Pt cluster can be changed into more attractive and repulsive bonding characters by adsorbed oxygen. On the other hand, the bonding interaction of Ni(core)-Pt(shell) bonds in Ni@Pt cluster under oxygen presence would always developed into repulsive bonding character, hence, weakening their bonding strength.

Table of Contents

List of Figures

List of Tables

Chapter 1

Introduction

1.1 Background and problems

In term of fuel efficiency, diesel engine is still more superior to gasoline engine. This also could be one of the economic reasons why diesel engine is widely utilized in car, bus, and truck for delivering people and goods. Despite the development of new generation diesel engine has been able to reduce the exhaust gas outputs significantly, the remaining untreated harmful gasses such as carbon monoxide (CO), nitrogen monoxide (NO), and unburned hydrocarbons (HC) are still posing a potential threat to the environment and human health. In addition, diesel engine also produces fine particulate matter (PM) with average size less than 2.5 μm that could cause detrimental effects to human respiratory and cardiovascular systems [1].

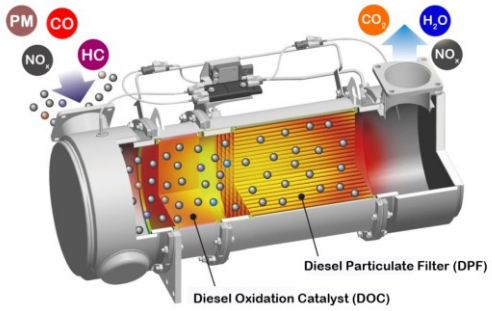

Figure 1-1 Schematic diagram of integrated DOC and DPF devices [2].

To tackle the environmental issues above, a device known as gas after-treatment system is introduced. The system consists of three main parts, they are diesel oxidation catalyst (DOC), diesel particulate filter (DPF), and selective catalyst reduction (SCR). Each component is responsible for certain types of works. As can be seen in **Figure 1-1**, the main function of DOC is to oxidize CO, NO, and unburned HC into CO_2, NO_2, and H_2O. These oxidized gases would later flow through DPF and utilize NO_2 as a burning fuel to combust and eliminate dangerous PM. In the process, NO_2 will be reduced back into NO where it finally would be retreated in SCR for the second time to be converted into nitrogen gas (N_2). DOC is usually made of small Pt nanoparticles that dispersed homogenously on

ceramic support γ-Al_2O_3 (111) surface. There are two reaction mechanisms that commonly used in explaining the catalytic oxidation processes in DOC, they are Langmuir-Hinshelwood and Eley-Rideal mechanisms [3, 4]. The details of the reaction steps for each mechanism and their exact differences can best be presented by an example of CO oxidation process on Pt(111) surface as shown below (**Figure 1-2**) [5].

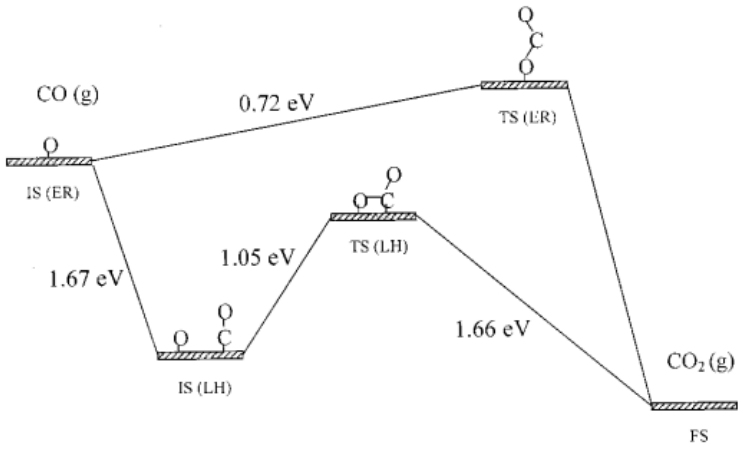

Figure 1-2 CO oxidation on Pt(111) surface via both the Langmuir-Hinshelwood (LH) and Eley-Rideal (ER) mechanisms

The problem that currently faced by commercial DOC is more heavily burdened by economic reason than of technological issue [6,7]. The economic issue is related to the sustainability and affordability of platinum resources in the market because from year to year the platinum price is steadily increasing due to high demand from industries is not followed by an ample platinum supply. This high platinum price eventually would also raise the production cost of DOC. In order to suppress the production cost as low as possible, lowering down the amount of Pt loading in DOC by reducing the size of platinum into several nanometers has been considered to be the current viable strategy. However, the method still has several drawbacks because of the fact that smaller Pt nanoparticles are notoriously susceptible to oxygen poisoning [8–11] aside from other major issues such as sintering [12] process. **Figure 1-3** confirms the statement above by showing that the NO conversion and NO turn over frequency (TOF) rates are proportional to the size of Pt nanoparticles that being implemented. Thus, the reason for the higher TOFs for NO

oxidation on larger Pt nanoparticles could be that, both thermodynamically and kinetically, larger Pt nanoparticles may be more difficult to oxidize, or they may interact more weakly with oxygen than the more open surfaces such as smaller Pt nanoparticles.

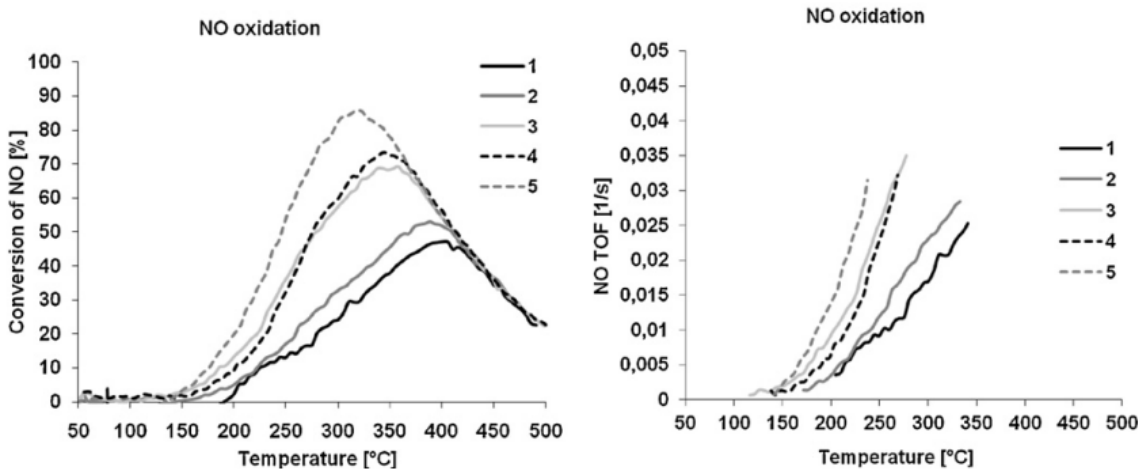

Figure 1-3 NO conversion and NO TOF over samples 1-5 exposed to 1000 ppm NO + 10% O_2 + 5% H_2O. Samples 1-5 refer to Pt particles sizes with 1, 2, 3, 5, and 10 nm [9].

1.2 Objective and thesis outline

From experimental result above, robust Pt-O bonds are considered to be the main cause that renders lower NO oxidation on small Pt nanoparticles. Although this simple underlying explanation is widely accepted as pointed out by many early studies, there is still lack of understanding regarding Pt-O bonding interaction on small Pt nanoparticles due to its complexity. Therefore, the main objective of this study is to conduct a thorough investigation on the mechanism of bonding interaction between small Pt clusters and oxygen in effort to find the best solution to avoid oxygen poisoning and if possible reduce Pt loading in DOC. For this purpose, the direct implications of geometry, size and alloying effects on small Pt clusters are discussed. Most of the current work here is carried out on non-supported Pt clusters excluding the first chapter of this study for the sake of computational cost as the size of Pt clusters are increased. The flow of discussion in this study is categorized into three main parts and explained as follows.

The first study discusses the influence of Pt cluster geometry and Al_2O_3 support on the reactivity of small Pt clusters by performing NO adsorption process on two Pt_4 isomers (tetrahedron and planar rhombus). NO molecule is used to measure the reactivity of Pt_4 clusters instead of oxygen based on the following considerations: (1) to compare the result with previous molecular dynamics calculation on tetrahedron-structured Pt_4 cluster [13]; and (2) early DFT result on isolated Pt_x clusters (x = 1-5 and 10) [14] shows that Pt clusters can bind NO much stronger than either atomic and molecular oxygen. Although these Pt_4 isomers may share similar atom number, their distinctive structures might cause certain Pt_4 isomer could generate weaker Pt-N bond, while the other one might exhibit stronger Pt-N bond. In addition, the comparative study between Pt_4 clusters that coated on Al_2O_3 surface and the ones in isolated (gas-phase) state would give valuable information regarding their reactivity and the stability of their attachment onto Al_2O_3 interface.

The second part of this study investigates the contribution of cluster size and reconstruction effects in adjusting the activation energy barrier of O_2 dissociation that absent from the discussion of previous theoretical studies. [15–17] The results of this study are expected to be able to elucidate the mechanism that initiates geometry reconstruction in small Pt clusters. The complete knowledge about this mechanism is needed in order to have better comprehension in evaluating and designing small Pt clusters that have lesser susceptibility to oxygen-induced reconstruction. For this purpose, the electronic properties of Pt-Pt bonds will be scrutinized further. Moreover, understanding the fundamental mechanism how cluster that undergoes structural deformation could promote oxygen dissociation without experiencing any energy barrier is imperative since O_2 dissociation process with lesser or no energy barrier leads to smooth formation of robust Pt-O bonds, and these bonds are considered to be the main source of oxygen poisoning that commonly occurred in small Pt clusters.

The last part of this study is mainly concentrated on core-shell Ni@Pt clusters which proposed as a prospective candidate for new DOC. This work is encouraged by the existence of bimetallic $NiPt/A_2O_3$ catalyst that experimentally has been proven to possess better catalytic reactivity in dry reforming of methane (DRM) [18,19], ethanol steam reforming [20,21], and hydrogenation of maleic anhydride (MA) [22] processes. In addition, the given catalyst has been demonstrated for being able to operate at higher

temperatures, which is mandatory for the operational working temperature of DOC during NO oxidation. Deliberately, we chose core-shell Ni@Pt nanoparticles as a suitable alloyed type of Ni-Pt catalyst for DOC based on the consideration that nickel has strong affinity towards oxygen and surface with high-coverage of Ni atoms could form robust Ni-O bonds stronger than do Pt-O bonds which would further accelerate the deactivation of the catalyst (oxygen poisoning). [23] Before performing a complete NO oxidation process analysis, it should be preceded by a judicious measurement test such as verifying whether the replacement of Pt clusters with core-shell Ni@Pt clusters would be able to significantly reduce the bonding strength of Pt-O bonds or not since Pt-O bonding strength is determining factor that regulates the next reaction steps in NO oxidation process. Lastly, it is also important to analyze the effect of surface reconstruction on bonding interaction at Ni/Pt (Ni@Pt) interface in order to check their bonding stability

Chapter 2

Geometry and Support Effects on Small Pt Clusters

In this section, the effects of geometry and support on the reactivity of small Pt clusters will be discussed. Understanding the role of these two effects would be expected to give valuable information and strong foundation in designing and tuning the reactivity of small Pt clusters. In this study, NO molecule is used instead of oxygen as an indicator of the catalytic reactivity of Pt_4 clusters where the reason has been given in the previous chapter.

2.1 Geometric structure effect on the reactivity of P_4 clusters

Recent experimental studies which performed in Fourier Transform Ion Cyclotron Resonance Mass Spectrometer (FT-ICR MS) [24–27] show that for clusters of less than 10 atoms, the cationic Pt clusters normally have higher reactivity as compared to the anionic Pt clusters. However, for Pt_4 clusters, an interesting behavior was observed. The anionic Pt_4 cluster is more reactive as compared with cationic Pt_4 cluster. In comparison with theoretical works, it is confirmed that anionic Pt_4 cluster has planar rhombus configuration while cationic Pt_4 cluster has tetrahedron configuration. [24,27] However, the electronic states and geometry of these Pt clusters have not sufficiently clarified. By using density functional theory (DFT), several groups have proposed the structures of this system. [28–30] Despite of many DFT studies involved in platinum tetramer (Pt_4) isomers, there are still controversies with its ground-state structure. For instance, DFT studies of Pt_4 clusters have indicated that the planar rhombus configuration (two-dimensional structure) is more stable than tetrahedron, which represents a three-dimensional structure. [29,31–34] However, results obtained from other computational calculations show otherwise [16,35,36]. In addition, the experimental studies carried out using FT-ICR mass spectrometer device only investigated the chemical reaction between isolated gas-phase Pt clusters and reactant gases, no γ-Al_2O_3 system as the oxide support was taken into account [24–27]. The support effect may

have significant contribution to the catalytic reactivity of small Pt clusters. Previous computational study tried to elucidate the mechanism of NO adsorption on Pt_4 coated on γ-Al_2O_3(001) surface. However, this study focused on Pt_4 cluster in a tetrahedron configuration only, and fails to take into account other potential cluster geometries [13]. While another study was able to present a thorough investigation on the Pt_n clusters (n=2-5) grown on α-Al_2O_3 (001) surface, no reactant gases adsorption calculation was performed [37]. In order to evaluate and understand the geometry and support effects on the catalytic reactivity of Pt_4 isomer, we carried out a detailed investigation on the reactivity of two types of Pt_4 isomers: tetrahedron and planar rhombus configurations. Both are studied in isolated environment and in the presence of γ-Al_2O_3(111) surface as the support. Furthermore, we calculated the adsorption of NO molecule as an indicator to assess the catalytic reactivity of Pt_4 clusters. In addition, the bonding interaction mechanism between Pt_4 and γ-Al_2O_3 (111) surface will also be evaluated.

2.2 Computational Methods

Periodic spin-polarized DFT calculations were performed using generalized gradient approximation (GGA) with the electron-ion interaction described by Perdew-Burke-Ernzerhof (PBE) as implemented in the Vienna Ab–initio Simulation Package (VASP) code [38,39]. The pseudopotentials were employed to describe the effective core potentials and the valence electronic states are represented by a plane-wave basis set with kinetic energy cut-off of 400 eV. The Brillouin zone integration was performed using a grid of 5×5×1 Monkhorst-Pack mesh.

To construct the gas-phase of isolated Pt_4 clusters, the calculations were done by placing the clusters in a sufficiently large unit cell to prevent interaction between neighboring cells. We used simple cubic unit cell of length 26.4 Å on each side and the optimized cluster structures are shown in **Figure 2-1**. The cohesive energy, E_b , of the cluster is calculated using the expression $E_b = E_{Pt} - E_{Ptn}/n$, where E_{Pt} and E_{Ptn} are the total energy of the isolated single Pt atom and Pt cluster, respectively. The *n* notation is the total number of Pt atoms within the cluster. We obtained the E_b values for tetrahedron and planar rhombus geometries of 2.57 eV and 2.59 eV, respectively, in

agreement with L. Xiao et al [28] (2.68 and 2.62 eV) for the same geometries. Our result is also in agreement with that of C. Zhou et al [37] which reported the calculated binding energy for tetrahedron and planar rhombus geometries, 2.71 eV and 2.72 eV, respectively. The average Pt-Pt bond distance in Pt_4 cluster with tetrahedron configuration is 2.62 Å, while that of planar rhombus is 2.52 Å. For simplicity, we define Pt_4 clusters with tetrahedron and planar rhombus configurations as T-cluster and P-cluster, respectively. In constructing γ-Al_2O_3 (111) surface, we used the structure of γ-Al_2O_3(111) surface proposed by H. P. Pinto et al [40] with (2 x 1) supercell as depicted in **Figure 2-2**. Hence, 16 Al atoms and 24 O atoms composed a unit cell of 11.32 x 5.66 x 23 $Å^3$. In order to avoid the interactions in the z-axis direction between neighboring supercells, we have considered a vacuum layer of 16.2 Å. The Al and O atoms in the five topmost layers of the eight-layer γ-Al_2O_3 (111) slab were fully relaxed in all directions until the maximum atomic force is less than 0.01 eV/ Å.

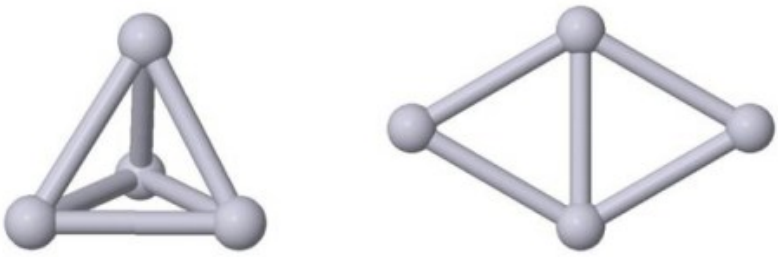

Figure 2-1 Pt_4 clusters with tetrahedron (left) and planar rhombus (right) configuration which are denoted as T-cluster and P-cluster, respectively.

As shown in **Figure 2-2**, the oxygen atoms on the surface form triangle and parallelogram-like patterns as highlighted with green and blue-dashed lines. The triangular patterns are labeled as tetra Al atop site (t-Alt), tetra O_S hollow site (t-O_Sh), and tetra O_S vacuum site (t-O_Sv). These three adsorption sites are expected to be more favorable since the T-cluster bottom plane has almost the same structure as shown in **Figure 2-1**, so when it is brought near the γ-Al_2O_3(111) surface, it makes the Pt-O distance relatively close and a strong bonding interaction can occur. In similar case, the parallelogram-like patterns are labeled as planar Al atop site (p-Alt) and planar O_S vacuum site (p-O_Sv). Based on **Figure 2-2**, it is obvious that these adsorption sites are

more favorable for P-cluster as the oxygen atoms on the surface formed a parallelogram-like pattern resembling the P-cluster geometry. The two topmost layers in the γ-Al_2O_3 (111) surface as well as the Pt_4 clusters were fully relaxed. The adsorption energy of the Pt clusters on the alumina surface was calculated using the following expression, $E_{Ptads} = (E_{sur} + E_{Pt}) - E_{Pt/sur}$, where $E_{Pt/sur}$ and E_{sur} are defined as the total energies of the alumina surface with and without the presence of Pt_4 clusters, respectively, where E_{Pt} is the total energy of isolated Pt_4 clusters. The NO adsorption calculation was performed on the most stable configuration of Pt_4 /Al_2O_3 (111) system for both Pt_4 clusters. The adsorption energy of the NO molecule on Pt_4 cluster coated on γ-Al_2O_3(111) surface was calculated using the following expression, $E_{NOads} = (E_{Pt/sur} + E_{NO}) - E_{NO/Pt/sur}$, where $E_{NO/Pt/sur}$ and $E_{Pt/sur}$ are the total energies of the Pt_4/Al_2O_3(111) surface with and without the presence of NO molecule, respectively, and E_{NO} is the total energy of isolated NO molecule. Furthermore, NO adsorption calculation was carried out on isolated Pt_4 clusters. Similar NO adsorption sites are applied for the isolated Pt_4 clusters. The NO molecule and all atoms in Pt_4 clusters except one Pt atom were fully optimized. The adsorption energy of the NO molecule on isolated Pt_4clusters was calculated using the following expression, $E_{NOads} = (E_{Pt} + E_{NO}) - E_{NO/Pt}$, where $E_{NO/Pt}$ and E_{Pt} correspond to the total energies of the isolated Pt_4 clusters with and without the presence of NO molecule, respectively.

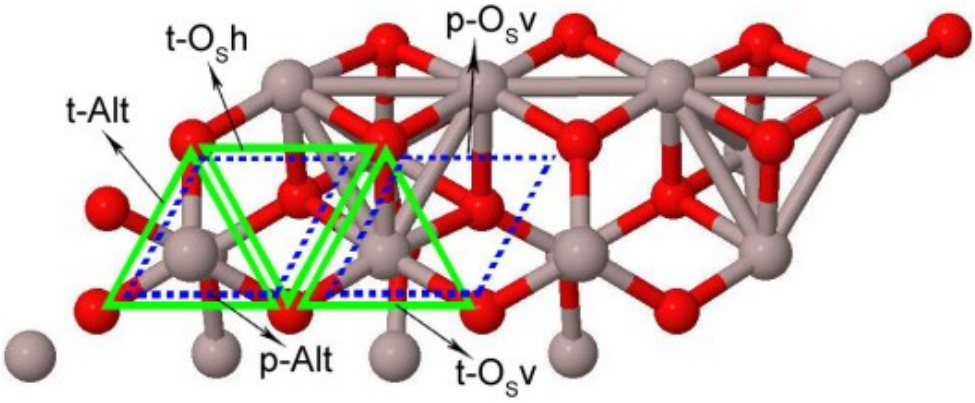

Figure 2-2 Supercell of γ-Al_2O_3 (111) surface (Top View). The red and gray spheres represent oxygen and aluminum atoms, respectively. Green and blue dashed lines represent the preferable adsorption sites for T-cluster and P-cluster, respectively.

2.3 Bonding interaction at Pt_4/Al_2O_3 interface

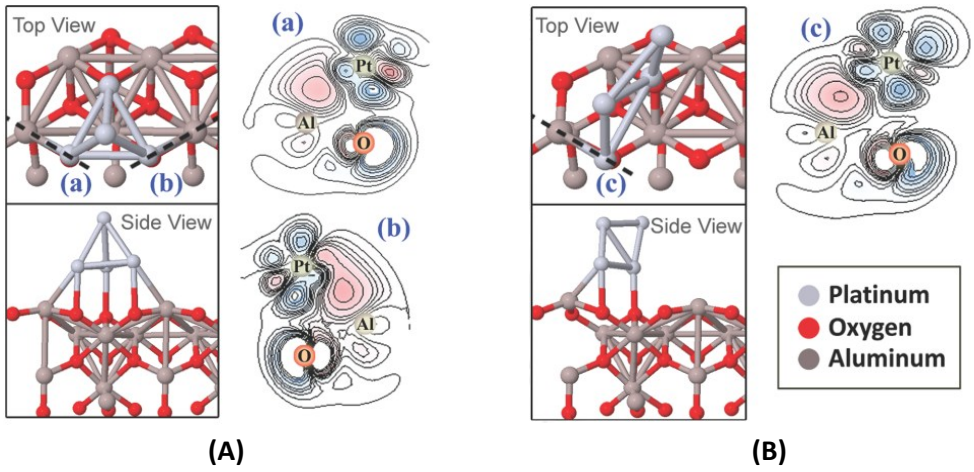

Figure 2-3 The most stable configuration of Pt_4 clusters coated on the γ-Al_2O_3 (111) surface. The **A** and **B** panels are T-cluster and P-cluster, respectively. The right side of each panel is charge density difference taken from the cross section plane marked by dashed black line in both clusters (Top view). The red and blue colors correspond to the attractive and repulsive interaction, respectively. The sphere with atom symbol is used to show the atom position.

The adsorption sites on γ-Al_2O_3 (111) surface for T-cluster and P-cluster are denoted by the green and blue-dashed lines, respectively, as shown in **Figure 2-2**. In **Figure 2-3**, the optimized structures for each geometry of Pt_4 clusters is presented along with their charge density difference profiles showing mainly the interaction between platinum, oxygen, and aluminum atoms. In **Table 2-1**, some important parameters related to Pt_4 clusters adsorption on γ-Al_2O_3 (111) surface is summarized. The "distance Pt_{bot}-O_{surf}" term refers to the average distance between platinum atoms and their nearest neighbor oxygen atoms. Our results show that the most favorable adsorption site for T-cluster is the t-O_Sv with the adsorption energy of -4.09 eV as depicted in **Figure 2-3** (left panel). While the second and third most stable configurations are t-O_Sh and t-Alt with adsorption energy of -3.65 and -2.43 eV, respectively (not shown). For P-cluster case, we found that it is strongly absorbed at p-Alt configuration with adsorption energy of -3.15 eV. After optimization, the P-cluster is more stable in upright position, almost perpendicular to the γ-Al_2O_3(111) and only two Pt atoms of P-cluster bond with the oxygen

atoms on the support as can be seen in **Figure 2-3** (right panel). Therefore, the T-cluster is found to be more stable on γ-Al_2O_3 (111) surface rather than P-cluster. This observation is explained as follows.

Table 2-1 Pt_4 Adsorption on γ-Al_2O_3 (111)

Adsorption Site	**E_{ads} (eV)**	**Distance Pt_{bot}-O_{surf} (Å)**	**Total charge on Pt_4 cluster**
t-Alt	-2.43	2.39	-
t-O_Sh	-3.65	2.36	-
t-O_Sv	-4.09	2.35	-0.28
p-O_Sv	-2.61	2.81	-
p-Alt	-3.15	2.23	-0.13

As shown in **Table 2-1**, both stable Pt_4 clusters on γ-Al_2O_3(111) surface have a slightly short Pt-O bond length, suggesting strong cluster-substrate bonding. The longer average Pt-O_{surf} bond length in t-O_Sv of T-cluster suggests that the p-Alt of P-cluster should be more stable on the support. However, the T-cluster is found to be the most favorable structure on γ-Al_2O_3 (111) surface, as mentioned above. This can be attributed to the contributions of Al-Pt bonding interactions. As shown in **Figure 2-3**, there are two Pt-Al bonding interactions in the Pt_4/Al_2O_3 (111) interface for T-cluster case, while there is only one Al-Pt bonding interaction in the P-cluster case. To further clarify the role of Al-Pt bonding interaction in the adsorption energy of Pt_4 clusters, we present the previous computational results that investigating the transition metal-Al_2O_3 interfaces [41,42]. According to these studies (see **Figure 2-4**), there are two main interactions that dictate the strength and quality of adsorption. The first one is the destabilizing O-metal interaction which is responsible for the weak (or even repulsive) adhesion energies found for oxide surfaces with high oxygen concentration. The second one is the Al-metal interaction where cationic Al atoms on the oxide surface are capable of forming strong bonds with the metal. These bonds resulted from interaction of empty Al dangling bond states with the d-band of the metal. In our case, this Al-Pt interaction would reduce the number of

electrons in the anti-bonding state (resulting from the interaction between O 2p and Pt 5d states) by transferring them to Al atom. And, the interaction from Al(3s)-Pt(5d) and Al(3p)-Pt(5d) hybridization would form a new bonding state that will stabilize and strengthen the bonding interaction between Pt_4 clusters and γ-Al_2O_3(111) surface. The more electrons transferred from the Pt to Al atom, the more stable the resulting interface is. If we take a closer look on the charge density difference profiles which are depicted in **Figure 2-3** (marked by (a) and (b) for T-cluster and (c) for P-cluster), it is obvious that there is a strong interaction between Pt and Al atoms as shown by high accumulation of electron density (red) near the Al atom. Moreover, Bader charge analysis verifies such observation as well. The Pt atoms in both Pt_4 clusters built from the bonding interaction with oxygen atoms in the γ-Al_2O_3 surface transferred electron to the support. On the other hand, the Pt atom that simultaneously makes bonding interactions with both Al and O atoms received electrons from the support. Due to the limitation of the Bader analysis method, we cannot define exactly which atoms on the top of γ-Al_2O_3 surface act as the electron donor. However, we are able to observe minimal electron transfer to Al atoms which directly make bond with Pt.

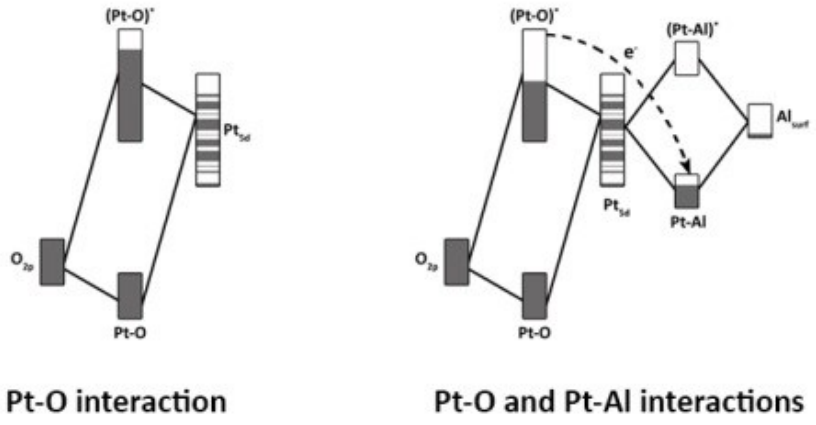

Figure 2-4 Schematic of bonding interaction between platinum and oxygen atoms without (left) and with (right) the presence of aluminum atom.

In summary, the overall charge transfer to Pt_4 clusters implies that both Pt_4 clusters withdraw the electrons from the support. This phenomenon also had been well explained

by V.R. Cooper et al [43]. In their study, the metal-oxide interfaces on two different kinds of α-Al_2O_3 surface were investigated by means of DFT calculation. For the Al-terminated surface, a charge transfer from the support to platinum atoms was noted, in contrast to the charge transfer from platinum atoms to the support which have took place if the surface is O-terminated. In our case, the γ-Al_2O_3 (111) surface is the Al-terminated surface, hence, agreeing with the results of this previous work.

2.4 NO adsorption on isolated Pt_4 cluster and Pt_4/Al_2O_3 surface

In order to verify the catalytic reactivity of Pt_4 clusters coated on γ-Al_2O_3 (111) surface, we chose NO molecule as the probe gas and performed the NO adsorption on Pt_4/Al_2O_3 (111) surface calculation. The choice for NO is mainly because of two main reasons, they are: (1) To compare the result with previous molecular dynamics calculation for tetrahedron-structured Pt_4 cluster case [13]; and (2) based on early DFT study on isolated Pt_x clusters (x = 1-5 and 10) [14], Pt clusters bind NO much stronger than atomic and/or molecular oxygen, hence, NO molecule can also be used as an indirect indicator of the reactivity of Pt_4 clusters towards oxygen.

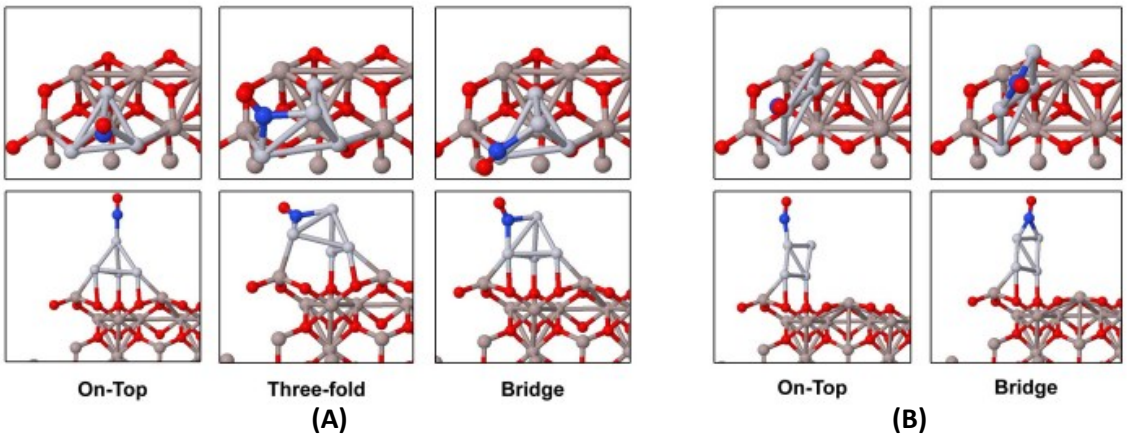

Figure 2-5 NO adsorption on Pt_4/Al_2O_3 (111) for T-cluster (A) and P-cluster (B) configuration, respectively. The top panel and bottom panel correspond to respective the top view and side view of the optimized structures.

Table 2-2 NO Adsorption on Pt_4/ Al_2O_3 (111)

Adsorption Site	E_{ads} (eV)	Distance N-O (Å)	Total charge on NO	Total charge on Pt_4 cluster
On-top(T)	-2.26	1.18	-0.18	-0.09
Three-fold(T)	-2.71	1.17	-0.29	+0.04
Bridge(T)	-2.86	1.22	-0.33	+0.13
On-top(P)	-2.99	1.18	-0.19	+0.08
Bridge(P)	-3.48	1.2	-0.28	+0.24

In **Figure 2-5**, we show the fully optimized NO adsorption on Pt_4/Al_2O_3 (111) surface for different adsorption sites. The nitrogen atom is oriented towards Pt_4 cluster instead of the oxygen atom, consistent with the previous studies [44–46]. For T-cluster case, three adsorption sites have been examined. Our results show that NO is strongly adsorbed on bridge site with the adsorption energy of -2.86 eV. These results are in good agreement with previous DFT and molecular dynamics calculation [13] where NO molecule prefers to be absorbed on the bridge site in Pt_4 cluster with tetrahedron configuration. For P-cluster case, there are only two possible adsorption sites, and our calculation gives similar result, that is, NO prefers to be absorbed on the bridge site, with adsorption energy of -3.48 eV. Between these two Pt_4 clusters (see **Table 2-2**), it is noted that P-cluster has higher reactivity as compared to the T-cluster. Unfortunately, direct comparison of these results with experiment is difficult since the anionic Pt_4 clusters results [24–27] are obtained from isolated gas-phase platinum clusters systems (no oxide supports such as Al_2O_3 are involved). However, we are able to make comparison between the experimental studies and the results of our computational study by conducting NO adsorption calculation on isolated Pt_4 clusters. In this calculation, we also performed the NO adsorption on the same adsorption sites as that of Pt_4/Al_2O_3 surface as depicted in **Figure 2-5**. In the isolated Pt_4 clusters system (**Figure 2-6**), the NO molecule prefers to be absorbed on the "on-top" site rather than on the bridge site as was found in Pt_4/Al_2O_3 (111) system for T-cluster case. This result is not quite surprising. Previous computational work [13] also had showed similar

result. However, for P-cluster case, despite of its isolated state, the NO molecule is still more favorable to be adsorbed on the bridge site with greater adsorption energy as compared to the results obtained from T-cluster case (**Table 2-3**). Also, we found that NO adsorption energies in both isolated Pt_4 clusters are slightly stronger as compared to that in Pt_4/Al_2O_3 (111) surface. This phenomenon is explained by the suppression of its catalytic reactivity when the Pt_4 clusters become saturated due to its interaction with the support. Moreover, the NO adsorption on P-cluster without support is still more stable as compared to that of isolated T-cluster. Similar trend is noted for P-cluster and T-cluster with support. One should then note that the isolated T-cluster possesses only three possible adsorption sites due to its high symmetric structure. Therefore, it is clear that there is no necessity to explore all the adsorption sites on T-cluster although such work may be useful for a more comprehensive study [31].

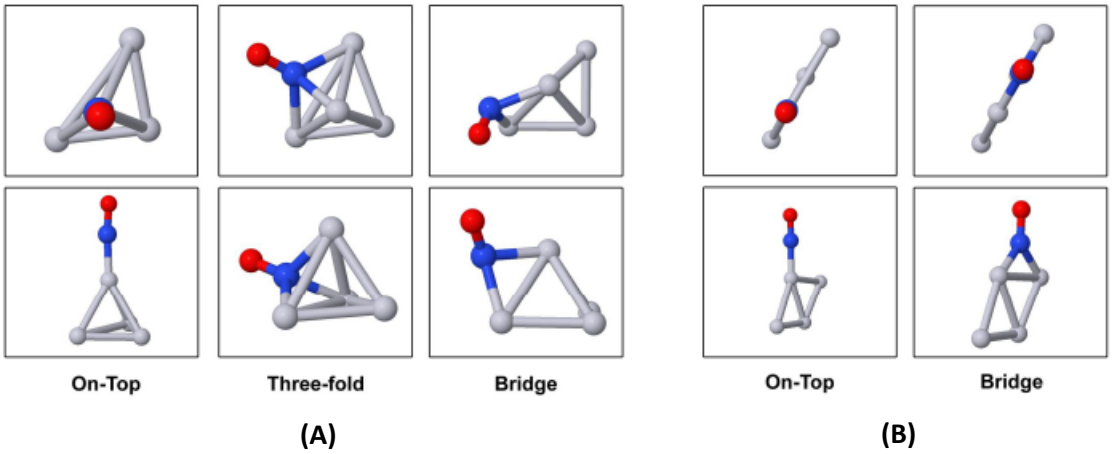

Figure 2-6 NO adsorption on isolated Pt_4 cluster for T-cluster (A) and P-cluster (B) configuration, respectively. The top and bottom panels show the top and side views of the optimized structures, respectively.

Table 2-3 NO Adsorption on Isolated Pt_4 Clusters

Adsorption Site	E_{ads} (eV)	Distance N-O (Å)	Total charge on NO	Total charge on Pt_4 cluster
On-top(T)	-3.02	1.18	-0.18	+0.18
Three-fold(T)	-2.04	1.21	-0.30	+0.30
Bridge(T)	-2.13	1.22	-0.27	+0.27
On-top(P)	-3.09	1.18	-0.19	+0.19
Bridge(P)	-3.46	1.22	-0.32	+0.32

To gain better understanding on the interaction between the adsorbed NO molecule (especially nitrogen atom) and the absorbent (either isolated Pt_4 clusters or Pt_4/Al_2O_3 (111) surface), the local density of states (LDOS) of both systems for the most stable configurations is presented in **Figure 2-7**. The positive (negative) value of the DOS corresponds to up (down) spin. The LDOS shown here are based on the condition where nitrogen atom has already formed bonds with platinum atoms in Pt_4 clusters. First, the LDOS of isolated Pt_4 clusters is shown in **Figure 2-7(a)**. It should be noted that the LDOS of isolated T-cluster only describes the interaction between nitrogen atom and a single platinum atom, while that of isolated P-cluster shows interaction with two Pt atoms (**Figure 2-6**). The intensity peak energy in the isolated P-cluster case is higher as compared to the isolated T-cluster one. In both isolated T-cluster and P-cluster cases, we can see clearly a peak in the occupied states which are mainly dominated by Pt 5d states (black line) and N 2p states (red line) in energy range of -7 eV to -8 eV, showing a strong p-d hybridization. In addition, a second peak energy located at around -13.5 eV was observed only for isolated P-cluster case. This peak energy is coming from the interaction between 2s and 2p states of nitrogen atom with the 5d states of two platinum atoms. This explains why NO molecule in the isolated P-cluster was absorbed slightly stronger than the one found in the isolated T-cluster case.

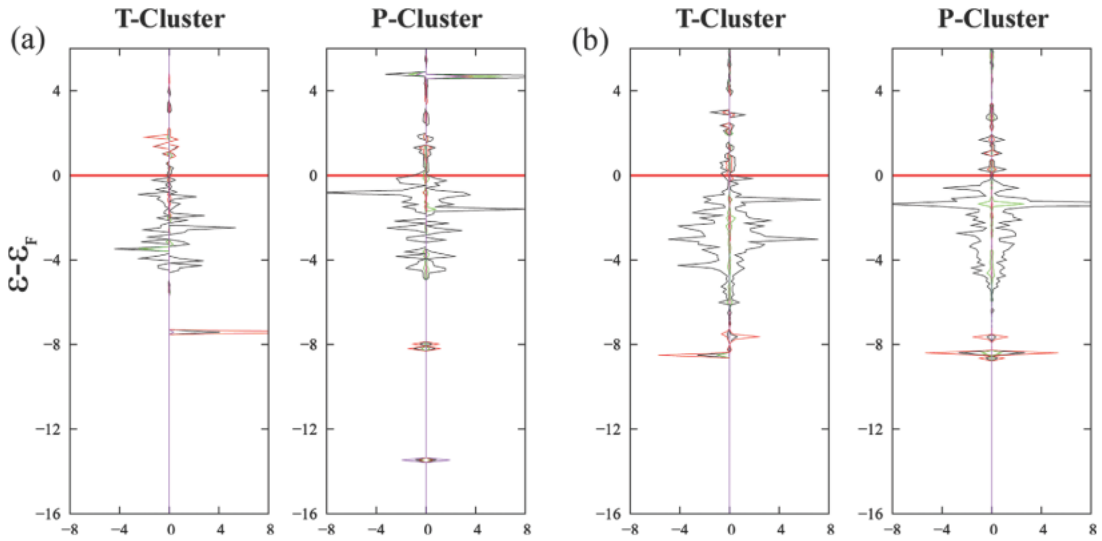

Figure 2-7 The LDOS describing the interaction between nitrogen atom and Pt_4 clusters (a) without and (b) with γ-Al_2O_3 (111) surface. The black, green, red, and purple color lines in the LDOS correspond to d-band (platinum), s-band (platinum), p-band (nitrogen), and s-band (nitrogen), respectively. The thick red line at zero is the Fermi level.

In Pt_4/Al_2O_3 (111) surface, the LDOS in both Pt_4 clusters (**Figure 2-7(b)**) also revealed a strong orbital hybridization of 6s and 5d states of two platinum atoms with the 2p states of nitrogen atom. The difference is that the intensity peak energy in P-cluster is more dominant and higher than those in T-cluster case. By comparing these two LDOS, it is clear which Pt_4 cluster configurations that more reactive towards the NO molecule. Hence, in general, we propose that the geometry of Pt_4 cluster on the support which is more reactive to NO may possess a planar rhombus configuration.

2.5 Summary

We have investigated NO adsorption process on two Pt_4 cluster geometries; tetrahedron and planar rhombus. Both of the calculations were carried out with and without the presence of γ-Al_2O_3 (111) surface as the support. The results show that Pt_4 anions cluster, which is considered to be the most reactive Pt_4 isomer based on mass spectroscopy measurement result, might possess planar rhombus geometry. This statement above is supported by the fact that the strongest Pt-N bond formation is found on isolated

planar-rhombus-structured Pt_4 cluster, not tetrahedron. Similar result is also found in the case of Pt_4/Al_2O_3 (111) surface where NO is more preferable to be adsorbed on Pt_4 cluster with planar rombus configuration on the bridge site like the one observed in isolated Pt_4 cluster although its adsorption energy is moderately reduced.

The NO adsorption on tetrahedron-structured Pt_4 cluster is weaker as compared to the planar rombus case in both isolated state and in the presence of Al_2O_3 support. This is actually a good indicator based on the consideration from DOC application perspectives because Pt cluster with higher catalytic reactivity may inflict adverse effect to NO oxidation process. In addition, tetrahedron-structured Pt cluster is also much stronger bonded to Al_2O_3 surface than the planar rhombus one, hence, the cluster is considered to be more favorable since it also has greater bonding stability at its Pt_4/Al_2O_3 interface. However, further experimental verification is still sought to check which one of these two isomers of Pt_4 clusters that more strongly adsorbed on the support and reactive towards NO molecule.

Chapter 3

Size and Reconstruction Effects on Pt-O Bonds Formation

As overview, this chapter presents the results of oxygen dissociative adsorption process on two types of isolated platinum (Pt) clusters: Pt_4 and Pt_{10}, by taking into account the effect of cluster reconstruction. The study highlights interstitial bonding orbitals (IBO) as one of two main factors that determine the strength of Pt-Pt bonds in the clusters and its vital role in cluster reconstruction during O_2 dissociative adsorption. Furthermore, the contribution of intramolecular forces between atoms in suppressing the rising energy barrier during oxygen dissociation process is explained.

3.1 Size-dependent cluster reactivity on small Pt clusters

For almost two decades of intensive research, the electronic properties of small Pt clusters have been known to be strongly influenced by several factors that define their inherited nature of catalytic reactivity such as size [47], ionicity [25], and support effect [48,49]. For instance, Andersson and Rosén [50] have conducted experimental study on O_2 molecules role in catalytic oxidation of hydrogen process on neutral Pt clusters. For the clusters comprised of 7 up to 30 platinum atoms, O_2 could work concurrently with H_2 to promote the formation and desorption of H_2O. Whereas for platinum dioxide clusters (Pt_nO_2) with $n < 7$ atoms, no catalytic water formation was detected, implying deactivation process has taken place. The fact that platinum dioxide clusters for $n \geq 7$ atoms could still be active in promoting water formation indicates that bigger clusters have different reactivity than smaller clusters. This confirms that cluster reactivity is size dependent. Although it has been widely known that cluster deactivation is stemming from stronger Pt-O bonds, there is no delicate explanation regarding the Pt-O bond formation mechanism because of the limitation of spectroscopic techniques. Investigating the mechanism of Pt-O bonds formation on small Pt clusters with various sizes is expected to be able to clarify how cluster size affect the formation process which may also serve as a good reference for Pt-based nanoalloys clusters as a comparative study.

Here, we compare the energetics of O_2 dissociative adsorption on two models of Pt clusters. Based on the gas phase studies elaborated above, Pt_4 and Pt_{10} clusters are considered to be adequate and sufficiently representative for comparative study in elucidating the size-dependent cluster reactivity in small Pt clusters. Furthermore, both clusters, where Pt_4 may act as representative of under-coordination of Pt_{10} cluster, possess similar tetrahedral structure that will provide insights into how active sites such as low-coordinated edge and corner atoms are generally dictated by cluster size. In the present work, we take into account cluster reconstruction effect during Pt oxidation process based on consideration that oxygen can induce surface reconstruction [51] where small Pt clusters are more susceptible than the surface [16]. It also meant to give a decent description how structure distortion in Pt clusters could have significant role in assisting Pt-O bonds formation process or provocating fragmentation if such case exists. Complete oxidation of Pt clusters is deemed to be unavailing to the main purpose of this study and such computational effort has been given somewhere else [16]. To distinguish the reactivity of individual atom in the bare clusters in concert with an effort to locate favorable adsorption sites for oxygen, we had employed the electron localization function (ELF) method [52]. The Pt-O bonding sterngth will be assessed by local density of states (LDOS) analysis and binding energy of individual oxygen atoms in the clusters.

3.2 Computational Methods

Calculations of O_2 dissociative adsorption on Pt clusters were performed using generalized gradient approximation (GGA) with the electron-ion interaction described by Perdew-Burke-Ernzerhof [53] as implemented in the VASP code [39,54–56]. The ionic cores are represented by projected augmented waves (PAW). To describe the valence electronic states, the Kohn-Sham single electron wave function was adopted and expanded by plane-wave basis set with a kinetic energy cut-off of 400 eV. The effect of spin polarization in all total energy calculations was taken into account. For isolated Pt clusters calculation, a single Γ-point was used. Structural relaxations were stopped when the energy difference between two consecutive relaxations was less than 0.1 meV leading to a convergence of forces down to order of 1 meVÅ^{-1}.

The clusters were modeled separately in a simple cubic unit cell of 25 x 25 x 25 Å^3,

to avoid electrostatic interaction among periodic images. The tetrahedron geometry which had been confirmed to represent the lowest energy structure for both Pt_4 and Pt_{10} clusters (see **Figure 3-1**, top panel), agreed well with previous studies [16]. 3D-isosurface electron density plot of Pt 5d orbitals was attained by using electron localization function (ELF) method and the result was visualized with VASP Data Viewer program package [57].

Employing the same supercell, the O_2 dissociative adsorption on Pt clusters was carried out. Prior to this process, a preliminary study of oxygen molecule adsorption was conducted in order to determine the most preferable adsorption site on the clusters where the adsorbed molecular oxygen thereafter will undergo dissociation process. By implementing static potential energy surface (PES) calculation, the final state for dissociation could be resolved. Both the initial (molecular precursor) and final states of Pt-O_2 configuration in each cluster were optimized and prepared for further analysis. During optimization, one platinum atom in the clusters was held frozen in its position, and the remaining atoms were relaxed.

To allow cluster reconstruction during the O_2 dissociation, the climbing-image nudged elastic band (CI-NEB) method [58,59] was applied. Four images which connect the initial and final states geometries along a reaction path in intermediate state were considered adequate to achieve smooth minimum energy path (MEP). Geometries were considered optimized when the maximum force on all images was less than 0.01 eV/Å. The adsorption and dissociation energy barrier of molecular oxygen on the Pt_4 and Pt_{10} clusters are obtained $E_{ads} = E_{Pt_i/O_2} - (E_{Pt_i} + E_{O_2})$ and $E_{bar} = E_{TS} - E_{MPS}$, respectively, where E_{Pt_i/O_2} (i = 4, 10) is the energy of oxygen absorbed on the corresponding cluster; E_{O_2} is the calculated energy of the isolated oxygen molecule; E_{Pt_i} is the energy of the clusters; E_{TS} is the energy of the transition state for O_2 dissociation; and E_{MPS} is the energy of adsorbed oxygen molecule. The index *i* corresponds to the respective Pt clusters.

3.3 Cluster reconstruction and interstitial bonding orbital (IBO)

It has been known that oxygen molecule has tendency to lie down on low-coordinated edge and corner (vertex) atoms as confirmed by previous studies [60,61]. However, the exact explanation regarding the mechanism why oxygen molecule prefers those atoms is still questionable. Kim and Ganteför [62] through ultraviolet photoelectron

spectroscopy (UPS) spectra analysis has shown that excess electron in free Au anion clusters (Au_n^-) can turn those clusters which are initially "inert" to become chemically very active towards oxygen adsorption. The term of "excess electron" here is thought to refer to free (non-bonding) electrons which are located in the valence electronic levels of Au_n^- and can easily make strong overlap with the O 2p orbitals. We believe that this feature also appears in small Pt clusters and having information about the distribution profile of non-bonding electrons in Pt_4 and Pt_{10} clusters, may become the first step to unveil the reason why the reacvitiy of a cluster is different from one another.

Topological analysis of the ELF which was originally formulated by Becke and Edgecombe [52] is considered qualified for this task. In brief, Silvi and Savin [63] have proposed a classification of chemical bonds based on ELF into three basic types: bonding, non-bonding, and core. The interpretation of these chemical bonds in term of 3D plot ELF is manisfested into several partitions of the molecular space which is known as "basin of attractors" that are in a one-to-one correspondence with expected chemical bond properties. ELF has values between 0 and 1; large values ranging between 0.5 and 1 can be ascribed to bonding and non-bonding localized electrons and smaller values (< 0.5) imply that the electrons are delocalized.

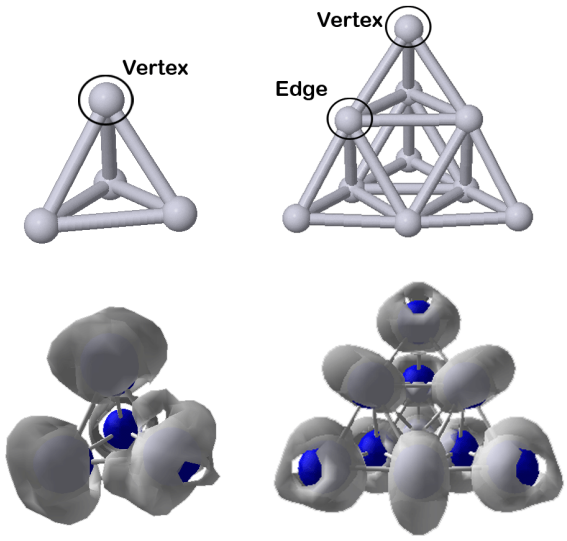

Figure 3-1 Optimized Pt_4 and Pt_{10} clusters configuration (top panel, left and right, respectively). 3D-isosurface of electron localization function (ELF) plots for Pt_4 and Pt_{10} clusters (bottom panel) shown by gray basin at $\eta = 0.17$. The blue spheres represent the position of Pt atoms.

In **Figure 3-1** (bottom panel), we plotted the 3D-isosurface of ELF for each corresponding Pt cluster (on top panel). The observed gray 0.17-localization basins that enclose Pt atoms give a distinct free electron density between Pt_4 and Pt_{10} clusters. These basins which reside in the valence regions are considered to be highly delocalized. Previoulsy, Gomez and coworkers [64] have shown that the electrons of small transition metal clusters M_4 (M=Pd, Pt, Cu, Ag, Au) have a strong delocalization character based on their ELF plots analysis. Therefore, our result is in good agreement with them. Moreover, the delocalized electrons in Pt clusters are mostly dominated by electrons from 5d orbitals because the 6s valence orbitals are more likely to be localized in the center of tetrahedron as underpinned by Goddard's interstitial bonding orbitals (IBO) model [65]. Our clusters also follow this role as we will explain later. Based on ELF description in both clusters, it seems reasonable for oxygen molecule to align its O-O bond axis laterally along the edge-bridge sites of Pt clusters since those sites accomodate a series of Pt atoms with dense accumulation of non-bonding electrons. A sequence of rigorous calculation has confirmed that the edge-bridge sites is the most reactive site as shown in **Figures 3-2(a)** and **3-2(d)** for Pt_4 and Pt_{10} clusters, respectively. The highest adsorption energy for oxygen molecule goes to Pt_4 which obtained 1.92 or 0.75 eV stronger than Pt_{10} (see **Table 3-1**). However, it is clear that the strength of Pt-O bonds does not correlate to the number of electrons that have been transferred from Pt 5d orbitals to anti-bonding O 2p orbitals. Bader analysis results reveal that adsorbed oxygen molecule in each cluster at MPS received the same amounts of 0.59 electron transfer.

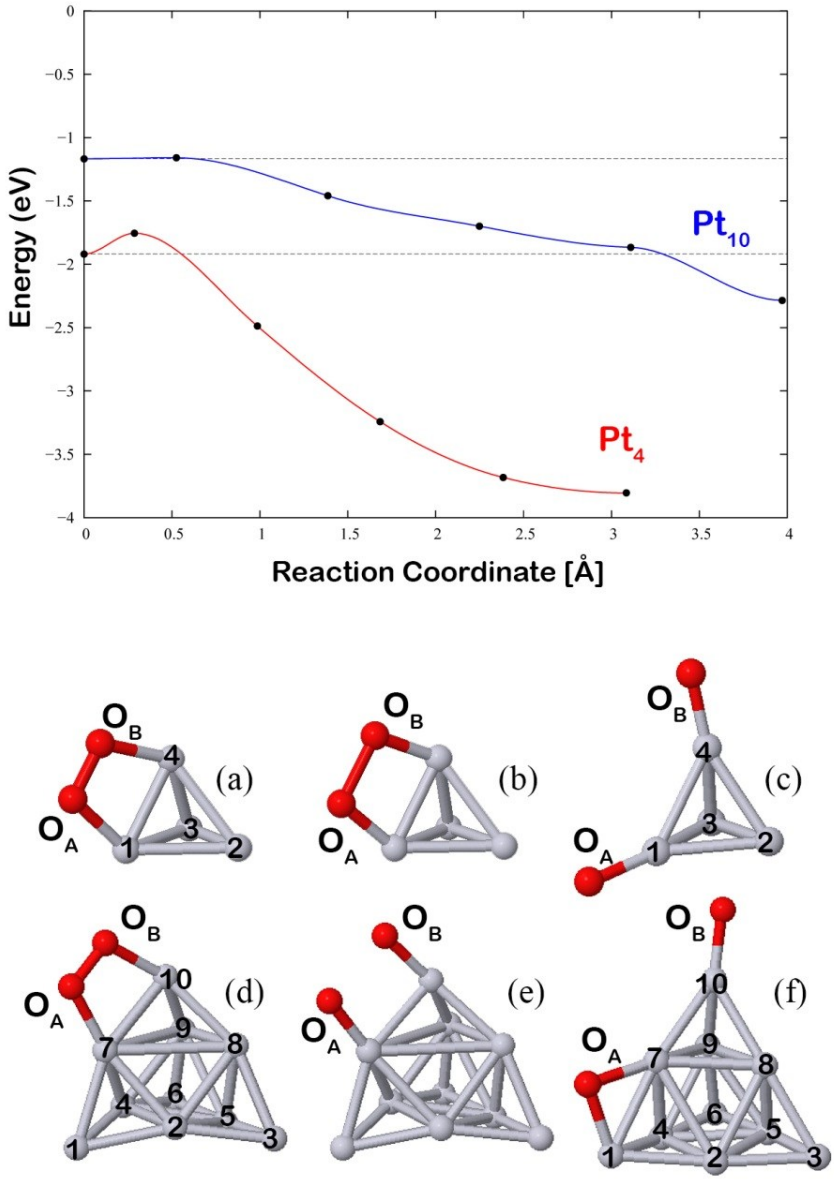

Figure 3-2 Oxygen dissociation process on the bridge site of Pt_4 and Pt_{10} clusters represented by red and blue lines, respectively (top panel). Energies are with respect to O_2 in the gas phase. The Pt_4 figures, denoted by (a)-(c), are corresponding to molecular precursor state (MPS), transition state (TS), and final state (FS), respectively. The Pt_{10} figures, denoted by (d)-(f), are also follow the same order. O atoms are red, and Pt atoms are gray.

Table 3-1 Oxygen dissociation process on Pt_4 and Pt_{10} clusters.

Cluster	State	Adsorption energy (eV)	O-O bond length (Å)	O_A-Pt (Å)	O_B-Pt (Å)	Barrier (eV)
Pt_4	MPS	-1.92	1.43	2.09	2.09	0.17
	TS	-1.75	1.78	1.86	1.87	
	FS	-3.8	5.17	1.77	1.77	
Pt_{10}	MPS	-1.17	1.41	1.96	1.98	0.01
	TS	-1.16	2.2	1.81	1.81	
	FS	-2.28	5.56	1.95[a)]	1.77	

Note: [a)] Average bond length of two Pt-O bonds.

From **Figures 3-2(a)** and **3-2(d)**, we can also see that the clusters especially Pt_{10} have experienced considerable geometry distortion. Oxygen that landed and bonded on Pt clusters consisting of only a few atoms has been proved to trigger geometry distortion in the clusters and develop new stable configuration of Pt oxides [16]. In Pt surface, similar phenomenon has also been clearly pointed out by Feibelman [51] despite of its utterly small effect to the surface reconstruction. Hence, most of DFT studies have neglected it and only consider the level of surface coverage [66,67] and favorable adsorption sites [68,69] as important aspects in dictating O_2 dissociation process. Here, we would like to propose one possible factor that is considered to have significant role in inducing cluster reconstruction. In **Figure 3-3**, we have depicted IBO at the states where the clusters are in their isolated state (a) and with absorbed oxygen attached on one of their edge-bridge sites (b). In isolated state, s-like IBO are formed in the interstitial region of tetrahedron structure at energy levels of -5.89 eV (Pt_4) and -6.86 eV (Pt_{10}) with respect to the Fermi level. Pt atoms which build stronger IBO are more likely to have shorter bond distance as can be seen clearly from the vertex atoms in Pt_{10} where they have the shortest bond distance with their first nearest neighbors as compared with Pt_4 case (see **Table 3-2**). This result agrees well with previous work that conducted by Kua and Goddard [65] but they did miss one d-like IBO which is formed in the center of octahedron structure in Pt_{10} cluster. The existence of d-like IBO has also justified the ELF plots result (in **Figure 3-1**) in which the edge Pt atoms in Pt_{10} cluster have lesser electron accumulation as compared with the vertex atoms owing to some of the 5d valence electrons that form IBO. Furthermore, when oxygen

molecule is absorbed on the clusters, the oxygen does not only weaken the d-d hybridzation between Pt atoms but also reduce the strength of IBO. For Pt_4 case, the weakening of IBO is not really significant and the cluster can still maintain its former structure although it becomes slightly distorted. In Pt_{10} cluster, the d-like IBO as the weakest one among others was believed to be the first IBO that get broken and force it to recombine with one weakened IBO (the s-like IBO on its top) to prevent further geometry deformation. From here, it is clear that the IBO act as the backbone of the cluster's geometry structure, when their bonding strength is reduced the cluster will easily get distorted to the some extent of geometry deformation.

Table 3-2 Distance between Pt atoms and number of neighbor atoms in Pt clusters.

Cluster	Coordination shell	Interatomic distance (Å)	Numbers of atom in each coordination shell
Pt_4 (vertex)	1	2.58	3
Pt_{10} (vertex)	1	2.54	3
	2	4.53	3
	3	5.08	3
Pt_{10} (edge)	1	2.54	2
	2	2.76	4
	3	3.91	1
	4	4.53	2

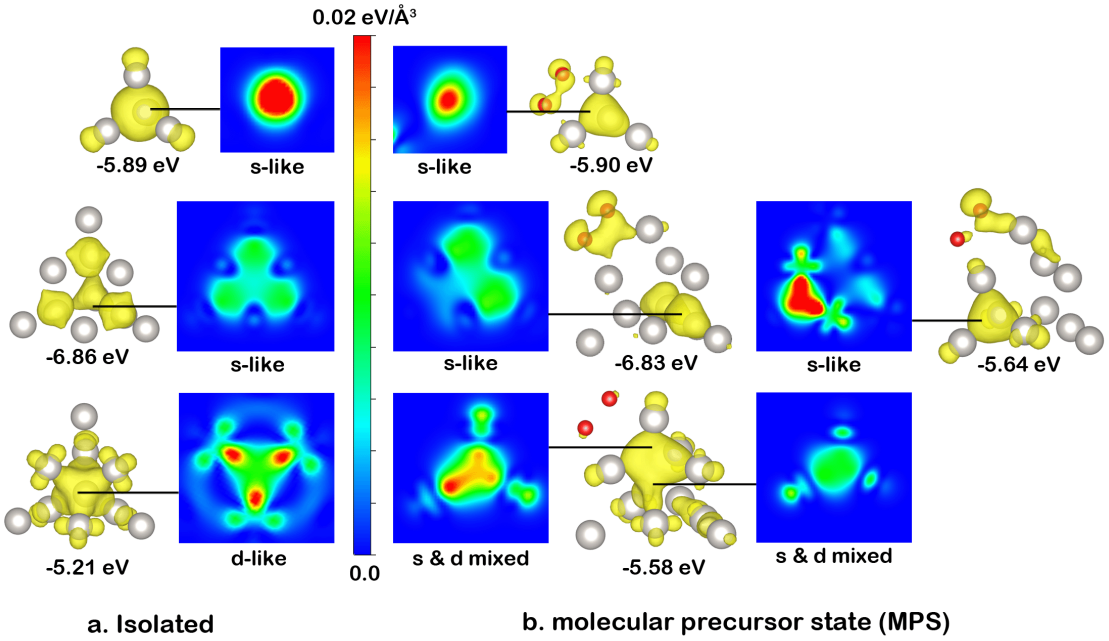

Figure 3-3 Interstitial bonding orbitals (IBO) in Pt_4 and Pt_{10} clusters: before (a) and after (b) reconstruction. The 3D-isosurface plots are portrayed at isosurface value of 7 m*e*/Å^3 and taken at certain energy level (which is given below of each cluster) with respect to the Fermi level. 2D-isosurface plots which are the horizontal cross section of corresponding 3D-isosurface are shown to clarify the profile of charge distribution intensity within IBO. Smaller (red) and bigger (gray) spheres are attributed to oxygen and platinum atoms, respectively.

As we have explained above, the reconstruction effect particularly in Pt_{10} case is obviously noticeable and shouldn't be ignored in consideration of geometry change in the clusters would also alter their electronic properties, consequently, it will affect the reaction path of oxygen dissociation process along the intermediate states. Hence, the oxygen dissociation process on Pt_4 and Pt_{10} clusters will be revisited to elaborate the influence of cluster reconstruction. To begin with, we concentrate our focus on oxygen which had been absorbed on each cluster molecularly (MPS). In more details, this oxygen either on Pt_4 or Pt_{10} have experienced a significant O-O bond elongation (see **Table 3-1**). The average stretched O-O bond length of 1.4 Å is a sign that can be interpreted as those oxygen species are more likely to be at *peroxo* state. To confirm our conjecture, we have calculated the vibrational frequency of oxygen at MPS and free gas-phase. The calculated free O_2 molecule in our system which has 1.24 Å bond length obtained $\nu = 1548.16$ cm^{-1}, in which, this frequency is relatively close to previous DFT work ($\nu = 1550$ cm^{-1}) [70] and the

experimental value (ν = 1555 cm^{-1}). [71] At MPS, the Pt_4 and Pt_{10} clusters gained 702.16 cm^{-1} and 747.59 cm^{-1}, respectively. Eichler and Hafner [68] have studied dissociative adsorption of O_2 on Pt(111) surface and their study indicates that the stretching frequency of O-O bond at peroxo state is 690 (710) cm^{-1} for a bond length of 1.43 (1.42) Å. Electron energy loss spectroscopy (EELS) results give ν = 700 cm^{-1} and ν = 710 cm^{-1} [71–73]. The vibrational frequency of oxygen in Pt_4 cluster matches almost perfectly with the value obtained from the experimental study. For Pt_{10} case, the value slightly deviates from Pt_4 which we presume to be a result of cluster reconstruction effect. Thus, it delivers a slight reduction on O-O bond stretching.

Next, a brief qualitative analysis of p-d hybridization at MPS will be presented. Based on partial (band decomposed) charge density calculation, several peaks below the Fermi level can be categorized into bonding and anti-bonding regions (divided by a solid green line, see **Figure 3-4**). Bonding-dominated region is composed of mainly constructive bonding interactions, and vice versa. It should be noted that the antibonding region is also occupied by some constructive bonding interactions, however, they have inferior significance in bonding share. In **Figure 3-4**, we present the LDOS of Pt_4 and Pt_{10} clusters at MPS where it describes "one-on-one" interaction of each oxygen atom in the absorbed O_2 molecule to the first nearest neighbour of Pt atoms. The first topmost LDOS is describing O 2p orbitals of free gas-phase oxygen molecule. The red, green, and purple lines are assigned to the total sum of projected O 2p orbitals, 2pσ, and 2p$\pi_{\parallel}$, respectively. The peaks of 2p$\pi_{\perp}$orbitals are overlaping with 2p$\pi_{\parallel}$ orbitals since both of them occupied the same energy level. A well-blended Pt 5d and O 2p orbitals characteristics which are expressed in narrow and sharp peaks are seen through Pt(1)-O_1 and Pt(4)-O_2 of Pt_4 cluster, while in Pt_{10} case, the peaks are a little bit broaden and blunt on some parts. The three predominant peaks at bonding dominated region, where O 2p orbitals (red) overpower Pt 5d orbitals (black) in intensity, are presumed to have compelling contribution to the bonding strength of Pt-O bonds. In overall, the p-d hybridization in Pt_4 cluster is slightly stronger than similar hybridization which is established in Pt_{10} cluster. Therefore, it confirms the trend that described by O_2 adsorption energy figure where the adsorption energy difference between Pt_4 and Pt_{10} clusters of 0.75 eV is deemed to be quite reasonable

considering the p-d hybridization profiles in both clusters do not have too much big difference as whole.

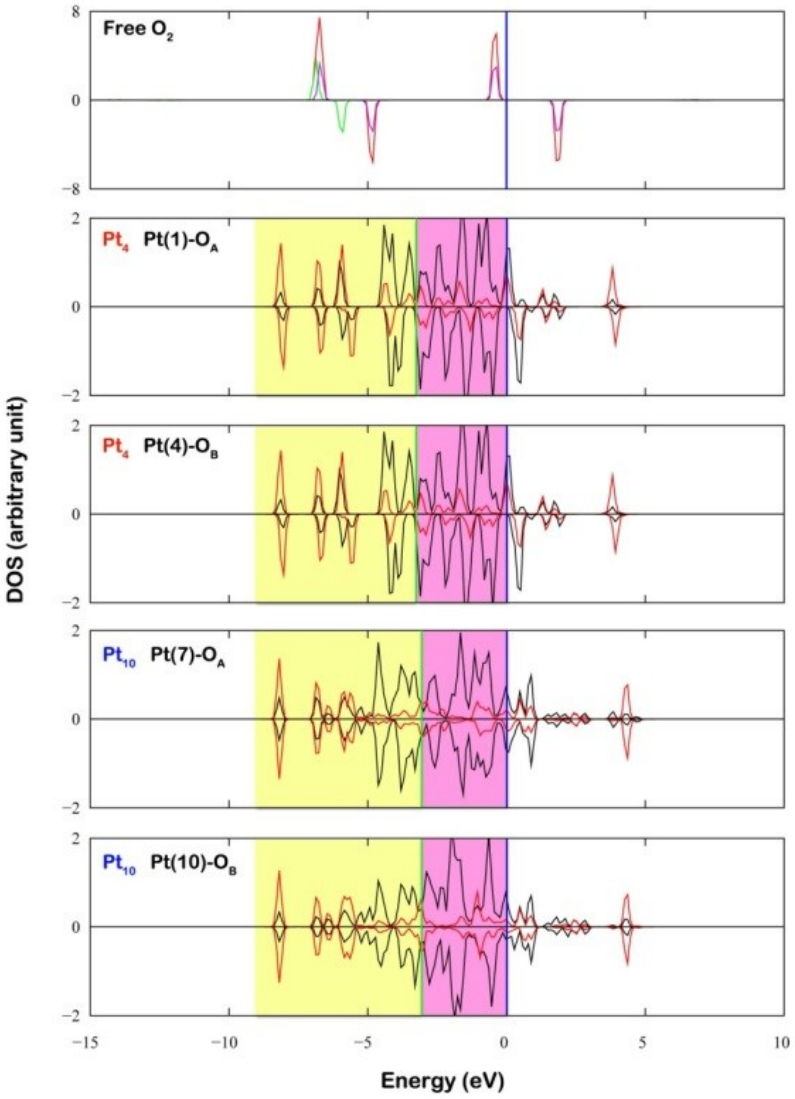

Figure 3-4 Local density of states (LDOS) projected into atomic orbital of free gas-phase oxygen and at molecular precursor states (MPS) which are describing p-d hybridization mechanism that occurred in Pt_4 and Pt_{10} clusters, respectively. The red and black lines correspond to respective O 2p and Pt 5d orbitals. The dark blue vertical solid line at zero is the Fermi level. The green solid line is the separator line between bonding (light color) and anti-bonding (dark color) regions.

3.4 Intramolecular forces and dissociation energy barrier

From Ci-NEB calculation results, we can locate the transition state (TS) for oxygen dissociation process in both clusters as summarized in **Figure 3-2** (top panel) where each geometry structure of the clusters at TS are shown in **Figures 3-2(b)** and **3-2(e)**. The data

are tabulated in **Table 3-1**. Visualisation of 2D-isosurface charge difference plots at TS (**Figure 3-5**) have confirmed that there is no electron accumulation detected in the near mid center of O-O bond axis in both clusters. However, to check whether these TS are the valid one, there are four criteria [74] that must be satisfied where one of them mandates the state which is presumed to be the valid transition state must have one and only one imaginary frequency. Our calculation confirmed that the vibrational frequencies in both clusters have one only imaginary frequency, they are 373.39i and 737.67i cm^{-1} for Pt_4 and Pt_{10} clusters, respectively. In Pt_4 cluster, the oxygen atoms vibrational movement posses symmetric stretching mode which is expected to be observed in the O-O bond breaking process. Strangely, the oxygen atoms in Pt_{10} cluster have asymmetric movement. In summary, there are three irregular characteristics that can be attributed to TS in Pt_{10} cluster: (1) the oxygen's imaginary vibrational frequency value is relative similar to its vibrational frequency value at peroxo state; (2) the oxygen atoms' vibrational mode doesn't show stretching (dissociation) mode (3) the O-O bond length at TS (2.2 Å) is longer than the one in Pt_4 case (1.78 Å). These discrepancies have caused ambiguity whether the TS that is gained in Pt_{10} cluster could be associated to O-O breaking process or if it refers to another "transition" process. To eliminate possibility of another missed TS, we have also conducted another Ci-NEB calculation for Pt_{10} case where only one image was used and it was put between MPS and TS along the reaction path. The calculation reveals a geometry structure where the O-O bond length is stretched as long as 1.88 Å which is quite close to the one found in Pt_4 cluster at TS, however the total energy is slightly lower -4.0 meV with respect to MPS. The result is, of course, invalid since energy of the transition state must be higher than that of the two states (MPS and FS) that it connects. Hence, we conclude that there is no energy barrier which required to break O-O bond in Pt_{10} cluster. The value of 0.01 eV that was gained at TS is merely a sudden energy fluctuation which, for instance, may have arisen due to an abrupt Hellman-Feynman force during atoms rearrangement as will be futher discussed below.

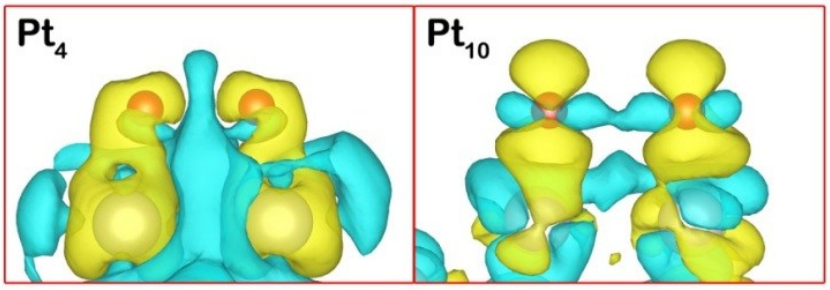

Figure 3-5 Charge density difference plots for Pt_4 (left) and Pt_{10} (right) clusters at transition state (TS). Yellow and blue smearing colors denote electrons accumulation and depletion, respectively. The atoms' colors are corresponding to similar designated elements which have been stated in caption of **Figure 3-3**.

In order to give a definite correlation how the distortions that occurred in clusters affect the quality of bonding interaction in Pt-O bonds particulary dissociation energy barrier, we will elucidate the connection between them in terms of force. The Hellman-Feynman force [75] that underpins attractive and repulsive forces between atoms or molecules is in general is formulated as

$$\nabla_\alpha \varepsilon_0(\vec{R}) = \langle \Psi_0(\vec{R}) | \nabla_\alpha H(\vec{R}) | \Psi_0(\vec{R}) \rangle \tag{3-1}$$

where the term on the left hand side defines the forces acting on any nucleus in any system as the gradient of the expectation value in ground-state $\varepsilon_0(\vec{R})$. The subscript α, $\vec{R}$, and Ψ_0 are corresponding to the α-th nuclei, 3D coordinate vector of nuclei α, and the electron wavefunction at ground-state. According to Feynman, [75] the hamiltonian H in its final form comprises the potential V which is made up of the interaction for each nucleus with an electron ($V_{\alpha i}$), and the interaction of nucleus with other nuclei ($V_{\alpha\beta}$). Hence, the equation above can be rewritten in more explicit expression as

$$f_\mu^\alpha = \int \sum_i \frac{\partial V_{\alpha i}}{\partial r_\mu^i} [\int i \int \Psi^* \Psi d\nu] d\nu - \sum_\beta \frac{\partial V_{\alpha\beta}}{\partial R_\mu^\alpha}. \tag{3-2}$$

The notation on the left hand side can be interpreted as the total force that acted on nuclei α where μ correponds to cartesian coordinates x, y, and z. The first and second terms on the right hand side are the attractive force between nuclei α with an ensemble of electrons and

the Coulomb repulsive force between nuclei α and nuclei β, respectively. One should notice that the attractive force of nuclei-electron varies as an inverse derrivation coordinate of electron i (r_{μ}^{i}). The repulsive force between nuclei changes is inversely proportional to the change in coordinate of nuclei α (R_{μ}^{i}). The main role of Hellman-Feynman force in structure optimization is to find the optimum equilibrium bond distance between atoms by preserving the total sum of attractive and repulsive forces that exerted on any nucleus in the system close to zero. In addition, it doesn't directly strenghten or weaken the binding energy between two atoms, however, if the distance between two atoms is too closer or far away from each other, it will also affect their binding energy. Thus, whenever one or more atoms in a cluster are shifted due to such external forces which are inflicted by incoming atoms/molecules, the cluster would try to bring back the balance through atoms rearrangement process that obeys the Hellman-Feynman force law.

Table 3-3 Intramolecular forces between atoms in P_4 cluster.

Atom	Force(eV/Å)		
	MPS	TS	FS
O_A	0.03	5.62	0.06
O_B	0.03	1.41	0.10
Pt (1)	0.02	3.59	0.06
Pt (2)	0.04	1.90	0.12
Pt (3)	0.04	1.69	0.09
Pt (4)	0.02	2.78	0.03

Table 3-4 Intramolecular forces between atoms in P_{10} cluster.

Atom	Force(eV/Å)			
	MPS	MPS-TS	TS	FS
O_A	0.11	0.01	0.03	0.03
O_B	0.11	0.01	0.02	0.02
Pt (1)	0.07	0.01	0.02	0.02
Pt (2)	0.12	0.00	0.03	0.03
Pt (3)	0.16	0.02	0.18	0.18
Pt (4)	0.26	0.01	0.01	0.01
Pt (5)	0.10	0.00	0.04	0.04
Pt (6)	0.19	0.01	0.05	0.05
Pt (7)	0.08	0.01	0.08	0.08
Pt (8)	0.12	0.01	0.06	0.06
Pt (9)	0.15	0.00	0.06	0.06
Pt (10)	0.16	0.01	0.04	0.04

From **Table 3-3**, we can see that the forces at MPS and FS are acknowledged to have an average value below 0.1 eV/Å, which means that the atoms are positioned on near equilibrium distance with each other. This condition is in contradiction with the forces that observed at TS where most of them have larger values above 1 eV/Å. Large force values at that state is coincidentally occurred at the same time the energy barrier reaches its maximum value. By deliberately comparing the force values with the one in Pt_{10} cluster (the fourth column in **Table 3-4**), there is a strong tendency that the rising of energy barrier would be followed by an increase in intramolecular forces magnitude. As the average force values at TS in Pt_{10} are generally well below 0.1 eV/Å, the energy barrier is also seem to be fairly low or negligible (which is only 0.01 eV). We have also calculated the intramolecular forces at the state between MPS and TS (the third column in **Table 3-4**), and the forces are proven to have similar low pattern values as one can compared side by side with either the force values in MPS or TS. Based on the analysis above, the mechanism of how the reconstruction can adjust the energy barrier can be explained as follows. Oxygen that undergoes dissociation process on small Pt clusters actually could avoid energy barrier if the clusters can accommodate O-O elongation by rearranging their atoms to maintain the balance of intramolecular force between their neighbor atoms. However, the stiffness of Pt atoms in the clusters is inflicting disproportionate intramolecular forces between the atoms where their margins with respect to the ideal (zero) force value are giving net restoring forces as listed in **Tables 3-3** and **3-4**. Any perturbation in the well-balanced attractive and repulsive forces between atoms is the main culprit which is responsible for the emerging energy (barrier) fluctuation. The reason is, first, oxygen on both clusters before reached MPS have underwent a partial dissociation process and their weak O-O bonds can be easily cracked with assistance of a modest external energy. Second, if oxygen in Pt_{10} could break its O-O bond without overcoming any energy barrier, we assume that the same situation could also work for Pt_4 case. However, it didn't happen because the movement of Pt atoms in Pt_4 is restricted by stronger s-like IBO, therefore, the atoms couldn't move as loosely as atoms in Pt_{10} cluster. On the other hand, broken d-like IBO and weakened s-like IBO which are induced by absorbed oxygen have granted Pt_{10} cluster more benefits to minimize the attractive/repulsive forces between atoms as low as possible

during O-O bond elongation. Of course, the claims that we made would still require further confirmation, but a previous study [76] has elucidated that diffusion energy barrier of oxygen to penetrate the interstitial site of metal oxides can be lowered if the surface atoms of the metal oxides can relax. The study implicitly supports the idea that atoms rearragenment/relaxing process can promote lower or no energy barrier during oxygen dissociation is possible.

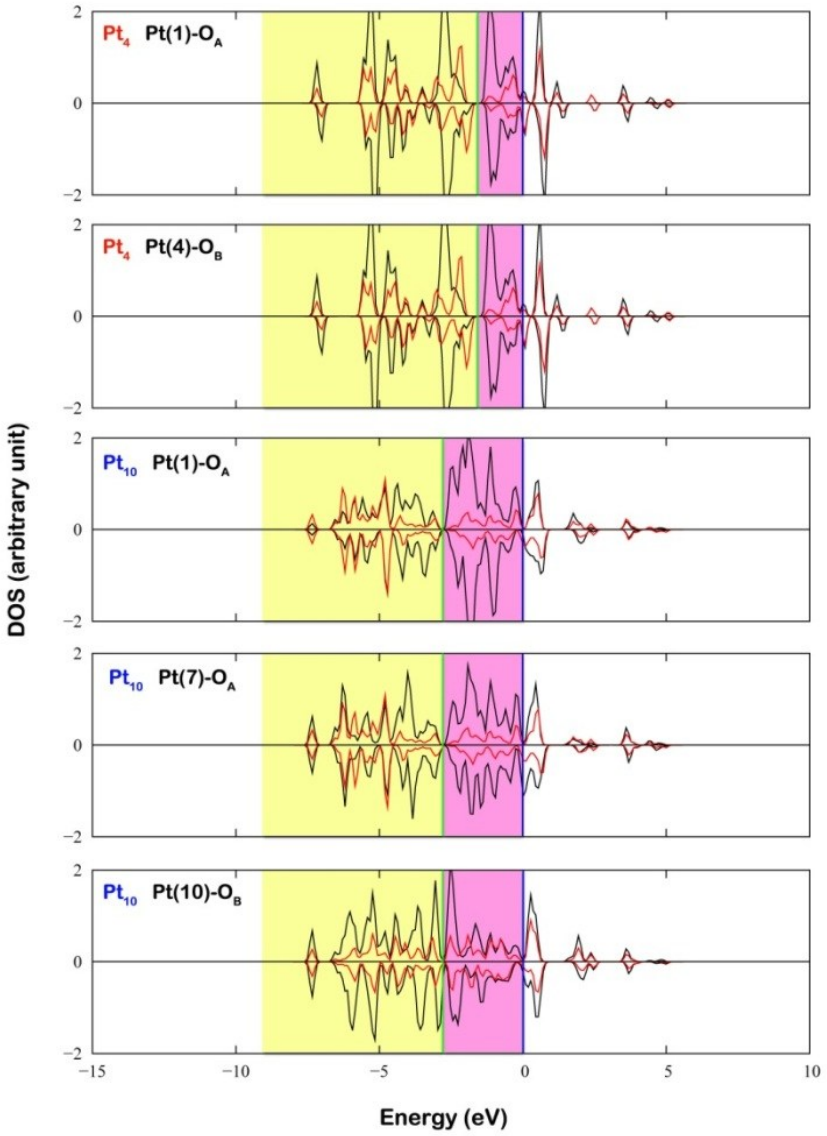

Figure 3-6 Local density of states (LDOS) projected into atomic orbital at final states (FS). For details please see caption of **Figure 3-4**.

Table 3-5 Oxygen atom binding energy at final state (FS)

Cluster	Designated oxygen atom	Binding energy (eV)
Pt_4	O_A	-5.42
	O_B	-5.42
Pt_{10}	O_A	-4.20
	O_B	-4.64

At FS, dissociated oxygen atoms would form stable Pt-O bonds as can be seen in **Figures 3-2(c)** and **3-2(f)**, and the strongest bonds are more likely to be developed in smaller Pt cluster as verified by the obtained oxygen adsorption energy (**Table 3-1**). Based on their LDOS description (**Figure 3-6**), the bonding-dominated region in Pt_4 cluster tends to become broaden while the antibonding region shrinks with explicit separation between them. Robust p-d hybridization that is characterized by several emerging peaks of 5d and 2p orbitals with striking narrow intensity at lower energy levels is implying that the strength of Pt-O bonds have been increased several times. On contrary, the p-d hybridization transformation in Pt_{10} case from MPS to FS is considered to be less significant. The vast majority of electron distribution of 5d orbitals in Pt_{10} excluding the Pt(10)-O_B case are still lying in antibonding region as can be noticed from Pt(1)-O_A and Pt(7)-O_B cases. Moreover, the peaks in general are still a little bit broaden, less intense, and not as narrow and localized as one may seen in Pt_4 cluster. These facts corroborate the notion that the bonding strength of Pt-O bonds in Pt_{10} is much weaker. The succinct LDOS analysis above might explain the occurrence in the oxygen adsorption energy at FS where Pt_4 gained the strongest Pt-O bonds (-3.8 eV) while Pt_{10} only obtained -2.28 eV. The gap is enormously big which has difference around 1.52 eV as compared with the previous one at MPS that only gives 0.75 eV.

As additional information, we find that the reactivity of the vertex atoms between both clusters is different based on oxygen binding energy measurement which is given in **Table 3-5**. This reactivity difference is in accordance with description of ELF plots that is previously shown in **Figure 3-1** (bottom panel). As we can see, the 3D-isosurface basins around the vertex Pt atoms in Pt_4 cluster are more bulky which tacitly declared that the atoms are more reactive than any vertex atoms in P_{10} clusters. Moreover, the edge Pt atoms

group in Pt_{10} has lesser basin density as compared with the vertex Pt atoms group which directly can be converted into a gesture that the edge atoms are less reactive than the vertex atoms. The validity of this explanation is supported by p-d hybridization profiles at FS (**Figure 3-6**), for instance, comparison between Pt(4)-O_B of Pt_4 and Pt(10)-O_B of Pt_{10} profiles. In correlation with coordination number, the basins expand as Pt atom has fewer nearest neighbor atoms (low coordination number) and it shrink when Pt atom has more nearest neighbor atoms (high coordination number) regardless the neighbor atoms are making direct or indirect bonding interaction with the atom. However, it should be noted that the coordination number that is obtained from EXAFS measurement cannot be linked to ELF plots because the number is representing reactivity of metal cluster as one entity body. It doesn't correspond to the reactivity of each individual of constituent atoms in that cluster. Nevertheless, the effectiveness of this ELF method is limited for small cluster only. For bigger clusters or surface, it might give a vague depiction since the electrons distribution on bigger clusters/surface tends to become more homogeneously distributed, hence, makes it harder to analyze.

3.5 Summary

In summary, this study demonstrates a simple O_2 dissociative adsorption process on Pt_4 and Pt_{10} clusters by taking into consideration cluster reconstruction effect. Oxygen that absorbed on the clusters already have weak O-O bond since it has partially dissociated, as the result, the bond can be easily cleaved. At the same time, the absorbed oxygen is weakening the IBO that serve as the backbone of the clusters' structure, and thus, triggering geometry reconstruction. Fortunately, it brings some advantages where Pt_{10} cluster can promote oxygen dissociation without experiencing any energy barrier. Further investigation shows that maintaining the balance of attractive and repulsive intramolecular forces between atoms is the main key to avoid any rise of energy (barrier) fluctutation. The energy barrier that gained in Pt_4 cluster is presumed to originate from the imbalance of intramolecular forces between atoms. Therefore, the dissociation energy barrier does not rise from the competition between attractive force that wants to hold O-O bond together and work which generated by oxygen atoms to break the bond. Furthermore, the ELF method is found to give an excellent coarse-grained picture of the reactiviy of individual Pt

atoms in the isolated clusters. This qualitative depiction from ELF serves well as a tool to predict favorable adsorption sites and which site in the clusters that would likely to form a robust Pt-O bond.

Chapter 4

Cluster Reconstruction and Its Effect on Bonding at Core/Shell Interface: Core-shell Ni@Pt and pure Pt Clusters

In this last chapter, alloyed Ni-Pt catalyst is being proposed as replacement of Pt in DOC. The main motivation comes from the fact that the current commercial DOC technology is still employing extremely expensive Pt metal as its active catalyst. Therefore, long-term research objective such as reducing Pt content in DOC while keep maintaining its catalytic oxidation performance has been considered to be the most critical issue for the sustainability of DOC. Deliberately, we chose core-shell Ni@Pt nanoparticles as the suitable alloyed type of Ni-Pt catalyst for DOC based on several considerations that will be given in the following discussion.

4.1 Core-shell Ni@Pt and pure Pt clusters

Platinum (Pt) has been playing a major role in diesel oxidation catalyst (DOC) consisting of platinum coated on Al_2O_3 support [77]. Due to its high cost and scarce resource, reducing the size of platinum into several nanometers has been considered to be a viable strategy in fabricating low-cost Pt/Al_2O_3 catalysts. However, the method still has several drawbacks because of the facts those smaller Pt nanoparticles are notoriously susceptible to oxygen poisoning [8], deformation [78], and sintering processes [79,80]. In recent years, several experimental studies have succeeded in synthesizing $NiPt/A_2O_3$ catalyst that has better catalytic reactivity in dry reforming of methane (DRM) [18,19], ethanol steam reforming [20,21], and hydrogenation of maleic anhydride (MA) [22] processes. This new type of catalyst is deemed to have a greater chance to improve and enhance the current catalytic oxidation of DOC. However, to the best of our knowledge, the catalyst has never been applied in DOC yet. One of the main hindrance in implementing the catalyst in DOC might stem from the uncertainties on how the Langmuir-Hinshelwood [3] and Eley-Rideal [4] mechanisms, which govern the oxidation processes in DOC, might proceed in the Ni-Pt catalyst. Another critical consideration is the appropriate mixing pattern of alloyed Ni-Pt metals. It has been well-known that nickel possess stronger affinity

towards oxygen and surface with high-coverage of Ni atoms could form robust Ni-O bonds stronger than do Pt-O bonds [23], hence, it would further accelerate the deactivation of the catalyst. Therefore, the design of new alloyed Ni-Pt catalyst is required to possess a geometric structure where its outer-most surface is highly dominated by Pt atoms rather than Ni atoms.

Core-shell Ni@Pt nanoparticle [81–83] is considered as a suitable solution that can satisfy the requirements above for three reasons: (1) The oxidation reactions would still be carried out on Pt-enriched surface, thus, it imposes no significant change to the general reactions mechanism that occurs in conventional DOC; (2) With a proper Ni:Pt stoichiometric ratio, nickel atoms could be covered almost perfectly by Pt atoms and refrained from making direct contact with oxygen; (3) Another potent advantage is as the size of the nanoparticles increases the shell-to-core atomic ratio decreases, consequently, less Pt loading would be needed in core-shell nanoparticles and reduction in Pt content is feasibly possible [81]. All of those benefits may give a solid justification to endorse core-shell Ni@Pt nanoparticles as a prospective catalyst candidate in DOC which is the aim of this present theoretical study.

Recent experimental study on Pt/Al_2O_3 [9] (**Figure 1-3**) shows that NO oxidation on the smallest Pt nanoparticle size (≈ 1 nm) was found to exhibit the lowest NO conversion and concomitantly the most sluggish turn over frequency (TOF). Early experimental work [84] has interpreted this sluggish TOF during NO oxidation due to stronger Pt-O bonds on smaller Pt nanoparticles as further confirmed by a DFT study [85]. In accordance to the objective of this study, it would be interesting and important to verify whether the replacement of 1 nm Pt nanoparticles with core-shell Ni@Pt nanoparticles of the same size would be able to significantly reduce the bonding strength of Pt-O bonds or not. Moreover, it is also interesting to clarify the effectiveness of compressive strain effect [86] on Pt-Pt bonds in Ni@Pt nanoparticles because there is always a higher possibility that the core-shell nanoparticles might experience a greater surface relaxation during Pt-O bonds formation. Therefore, in this preliminary work, we carry out density functional theory (DFT) calculation to examine Pt-O bonding interaction on 1 nm core-shell Ni@Pt cluster and also the influence of oxygen-induced cluster reconstruction in reshaping the distribution pattern of first nearest neighbor (1NN) Pt-Pt bond in the cluster. As we will

show later the change in 1NN Pt-Pt distribution that caused by adsorbed oxygen is a feature that closely comparable to the depiction of Fourier transformed EXAFS data during platinum oxidation process [87,88]. In addition, despite of advanced spectroscopy techniques in EXAFS have made this information readily becomes available, there are still some lacks of knowledge about how this cluster reconstruction affects the bonding interaction at Ni/Pt interface. This kind of bonding interaction is one of many important attributes of core-shell nanoparticles that experimentally difficult to be characterized in detail, yet need to be corroborated further. For this reason, oxygen-induced cluster reconstruction effect on the bonding at core/shell interface will also investigated. In order to build connection between theoretical model of Ni@Pt cluster and the EXAFS measurement above, (non-alloyed) pure Pt cluster of similar size was built as reference for side-by-side comparison with Ni@Pt cluster. Aside from computational cost and limitation considerations, 1 nm Pt cluster is of particular interest because such cluster has been experimentally synthesized and characterized as shown in many studies [9,48,89,90].

4.2 Computational Methods

To construct 1 nm nanoparticles, we adopted the so-called magic cluster (i.e., clusters containing complete shell of atoms) size of 55 atoms [91,92] and found that Mackay icosahedron is the most stable structure among other 55-atom Pt cluster isomers. In designing Ni@Pt cluster, we deliberately evaluated only one stoichiometric ratio of Pt:Ni that proportionally close to 3:1 considering this ratio can guarantee all surface atoms are composed of Pt atoms and while experimentally it has been demonstrated as the optimum ratio to achieve high catalytic reactivity in oxygen reduction reaction (ORR) [93]. Based on seminal DFT study that carried out by Wang et al [92], it is confirmed that the alloyed 55-atom Ni-Pt cluster is energetically more favorable to accommodate Pt-enriched surface. This allows us to construct Ni@Pt cluster where 42 out of 55 atoms are positioned on the cluster surface.

All the calculations were performed with the VASP program [38,39,54] using similar periodic cubic cell and parameters that used in calculating Pt_4 and Pt_{10} clusters in **Chapter 3**. The only difference is that the energies were converged to 1 meV/atom and ionic relaxations were allowed until the absolute value of force on each atom was below 0.02

eV/Å. All atoms, except one core atom in the center, were allowed to undergo full relaxation. In order to investigate oxygen-induced reconstruction effect, we have applied two different relaxation schemes for oxygen adsorption calculations, they are: (1) oxygen atom was relaxed and all atoms in the clusters were fixed; (2) oxygen and all atoms in the clusters, except one fixed atom, were fully relaxed.

The oxygen adsorption energy (E_{ad}) is calculated from the total energy difference between Pt cluster with oxygen ($E_{Pt\text{-}O}$), pure Pt cluster (E_{Pt}), and isolated oxygen (E_O) relative to $\frac{1}{2}O_2$ in gas phase (E_O) as given by the equation, $E_{ad} = E_{Pt\text{-}O} - (E_{Pt} + E_O)$ (For core-shell case, $E_{Pt\text{-}O}$ and E_{Pt} are replaced by $E_{Ni/Pt\text{-}O}$ and $E_{Ni/Pt}$, respectively). To obtain the oxygen vibrational modes, the oxygen atom was displaced from its equilibrium position where its displacement was regulated in accordance with density-functional perturbation theory (DPFT) method [94] and executed within VASP program. In this calculation, all metal atoms which built the clusters remain fixed because those atoms (Ni and Pt) have weight mass several times heavier than oxygen, therefore they would not be displaced as the oxygen atom vibrates. This approximation would only give a slight deviation to the oxygen vibrational frequencies.

4.3 Cluster geometric structure and oxygen adsorption energy

Figure 4-1 shows the optimized core-shell Ni@Pt (a) and pure Pt (b) clusters where the surface (shell) atoms arrangement gives 20 identical equilateral triangular faces and all of them share similar high-index (111) facet surface. With respect to the stable configuration of 13-atom Ni and Pt clusters [28,95], (see **Figure 4-1(c)**), the inner Ni-Ni bonds (a_0, a_1) of Ni@Pt cluster are stretched but the inner Pt-Pt bonds (a_0, a_1) of pure Pt cluster remains unchanged (see **Table 4-1**). Interestingly, the average shell Pt-Pt bond distances (a_4) of core-shell Ni@Pt (2.68 Å) and pure Pt (2.79 Å) clusters are closely match the values that obtained from X-ray diffraction (XRD) data, 2.70 Å and 2.77 Å, respectively [96,97]. However, the actual shell Pt-Pt bond distances in 55-atom cluster are not homogeneous, most probably, because there are two distinguishable shell Pt atoms which possess two different nearest neighbor atoms. As seen in **Figures 4-1(a)** and **4-1(b)**, those atoms are labeled by A and B letters which stand for atoms with low and high

coordination numbers, respectively. Furthermore, the average bond distances for A-B and B-B bonds in Ni@Pt case are 2.63 Å and 2.73 Å consecutively, while the obtained values in pure Pt cluster are 2.72 Å and 2.86 Å following the same sequence. It is obvious that all shell Pt-Pt bonds in Ni@Pt cluster are contracted due to the presence of Ni core atoms. In addition, the values of a_4 which are provided in **Table 4-1** are gained by taking the average value of A-B and B-B bond lengths.

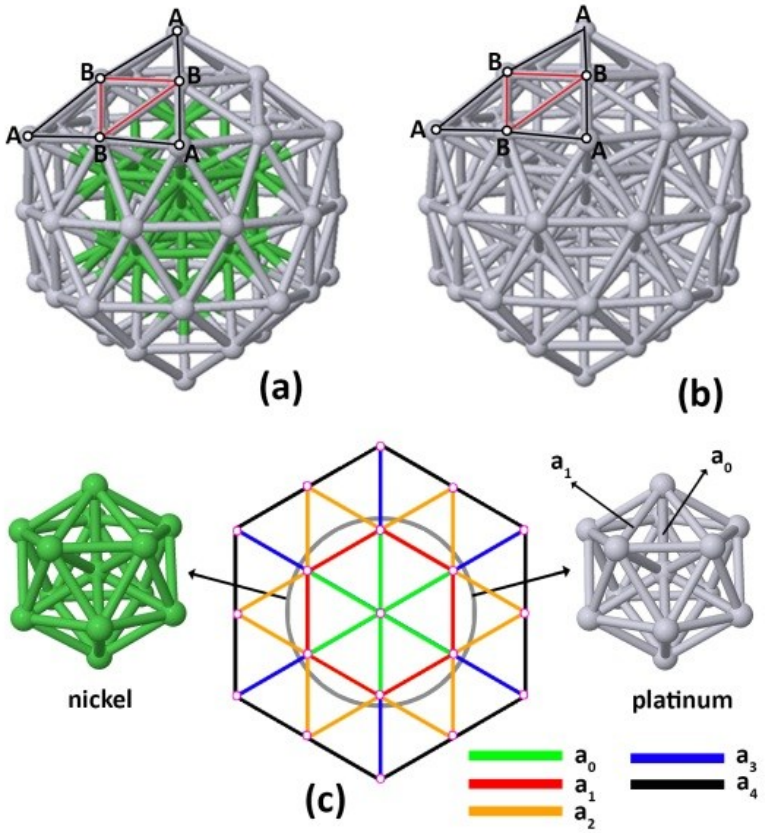

Figure 4-1 Optimized structures of core-shell Ni@Pt (a) and pure Pt (b) clusters with embedded red and black lines represent two varying Pt-Pt bond distances. The schematic cross-section of the clusters structure **(c)** exhibits the connecting bonds between atoms vary in length as indicated by characters a_n (n=0,1,2,3,4) where their values are provided in **Table 4-1**. The 13-atom clusters on the left and right sides serve as the core atoms of Ni@Pt and pure Pt clusters. Platinum and nickel atoms are represented by gray and green spheres.

Table 4-1 Atom-atom bond distances of the bonds in core-shell Ni@Pt and pure Pt clusters that shown in **Figure 4-1(c)** and denoted by characters a_n (n=0,1,2,3,4). The unit is given in Å.

	Ni@Pt	Pure Pt
a_0	2.40	2.62
	2.32*	2.63*
a_1	2.53	2.76
	2.44*	2.77*
a_2	2.69	2.76
a_3	2.59	2.54
a_4	2.68	2.79
Pt-Pt (exp)	2.70 (5 nm)	2.77 (3 nm)

*refers to the stable 13-atom cluster

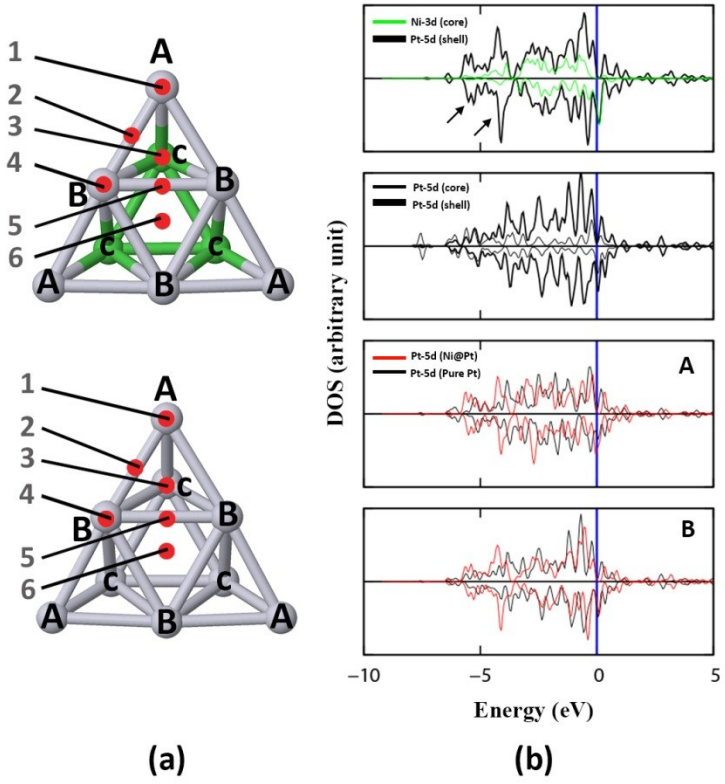

Figure 4-2 Small representative structures of core-shell Ni@Pt (top) and pure Pt (bottom) clusters (a) that are taken from the cluster shown in **Figures 4-1(a)** and **4-1(b)**. The numbers denote oxygen adsorption sites and the label **c** correspond to core atoms. The projected density of states (PDOS) of both clusters **(b)** is provided for total shell and core atoms (two topmost panels) and single atoms A and B (two bottom panels). Gray and green spheres are corresponding to platinum and nickel atoms.

Because the clusters have high geometric symmetry, investigation to locate the preferable adsorption sites for oxygen atom can be concentrated on one equilateral triangular face where 6 adsorption sites are considered as indicated in **Figure 4-2(a)** for each corresponding cluster. The 6 adsorption sites have taken into account all possibilities of Pt-O bond configurations that may exist. The oxygen adsorption energies are summarized in **Table 4-2** for each assigned site. For all sites, oxygen adsorption energies in pure Pt cluster are lower than those energies in Ni@Pt for either reconstructed or rigid cluster case. The trend of weaker oxygen adsorption energy in Ni@Pt cluster is mainly caused by the 5d states of shell Pt atoms on the surface strongly interact with the 3d states of core Ni atoms (see **Figure 4-2(b)**). Shifting the weight distribution of 5d states of Pt atoms (A and B) to lower energy region (as pointed out by the arrows) and leaving less available Pt-5d states that could interact with O-2p states. Hence, the shell Pt atoms in Ni@Pt cluster could not bind oxygen as strong as those atoms in pure Pt cluster. This strong Ni(3d)-Pt(5d) hybridization in Ni@Pt cluster is physically manifested in form of contracted surface Pt-Pt bonds due to bond distances mismatch at Pt/Ni interface which widely known as compressive strain effect. However, cluster reconstruction that occurs on Ni@Pt cluster could loosen the strained Pt-Pt bonds and increase oxygen adsorption energy. Similar result is also found in pure Pt cluster since the cluster's surface Pt-Pt bonds are also less rigid and their bond lengths can be easily deviated. According to Lu and Henkelman [98], oxygen-induced cluster reconstruction will stabilize the adsorbed oxygen and thus reduce the catalytic activity of Pt-based nanoalloys. The evidence is quite clear from **Table 4-2** where oxygen adsorption energies in reconstructed cluster for all site are lower than those (within parentheses) in rigid cluster.

Furthermore, the oxygen adsorption energies in the reconstructed pure Pt cluster, which are spanning between -3.45 eV to -4.60 eV, are quite reasonable in comparison with thermal desorption spectroscopy (TDS) work on Pt(111) surface [73] In that study, the heat of desorption at oxygen coverage ranging from 0.2 of saturated coverage into nearly zero is within the limit of 250-500 kJ/mol or equivalent to 2.59-5.18 eV. Further analysis provides that while majority of the adsorption sites give oxygen adsorption energies closer to or lower than -4 eV, oxygen atom that adsorbed on vertex B site has the weakest adsorption energy. In addition, the site number 5 (bridge B) is not favorable for Pt-O bonds formation

and oxygen on those sites are more likely to drift away to hcp-like sites during structural optimization. The reason could be the activation energy barriers of the reaction pathway between bridge B and hcp-like sites are minuscule, as consequence, the metastable adsorbed oxygen atom on bridge B sites could easily slide off to hcp-like sites.

Table 4-2 Oxygen adsorption energy and Pt-O stretching frequency on various designated adsorption sites as shown in Figure 4-2 for Ni@Pt and pure Pt clusters. The values within parentheses refer to oxygen adsorption energies in rigid cluster case.

cluster/ surface	Site number	Site position	Adsorption energy (eV)	frequency (cm^{-1})	Frequency gap (cm^{-1})
Ni@Pt	1	vertex A	-4.06 (-3.96)	787	54
	2	bridge	-4.51 (-4.18)	492[a]	
	3	hcp-like	-4.51 (-4.19)	546[a]	
	4	vertex B	-3.45 (-3.06)	722	
	5	bridge B	unstable		
	6	fcc-like	-4.22 (-3.91)	451	
Pure Pt	1	vertex A	-4.27 (-4.11)	752	73
	2	bridge	-4.51 (-4.30)	447[b]	
	3	hcp-like	-4.61 (-4.28)	520[b]	
	4	vertex B	-3.76 (-3.58)	725	
	5	bridge B	unstable		
	6	fcc-like	-4.55 (-4.14)	405	
Pt (335)	-	terrace	-	470[c]	90
(exp)	-	step	-	560[c]	
	-	step	-	700	
Pt_4	-	bridge	-1.75 (O_2)	666 (TS)	
Pt_{10}	-	bridge	-1.16 (O_2)	693 (TS)	

Note: the frequency gap is calculated by taking frequency difference between the sites that assigned by superscripts **a**, **b**, and **c**. TS is abbreviation for "transition state"

4.4 Adsorption site preference and stretching frequency

In stepped Pt(111) surface, the dissociated oxygen atoms are widely known to be attracted subsequently to edge-bridge > fcc > hcp > bridge > atop site [51,73,99,100]. Similar observation is also found in Pt(335) and Pt(321) surfaces. However, for 55-atom cluster case, as the definite boundary line that divides edge and three-fold hollow sites region becomes blurred, the oxygen adsorption energy gap between those sites is also getting smaller. Accordingly, the given adsorption energies are less reliable to draw the sequence of most-to-least-stable adsorption sites for oxygen atom in both Ni@Pt and pure

Pt clusters. Recently, potential energy surface (PES) that based on computational work on Pt(321) [101] has successfully elaborated the oxygen adsorption sites preference that previously proposed by HREELS and TDS measurements [102] where the results of both experimental and theoretical works lead to similar conclusions. For this reason, ν(Pt-O) stretching frequencies for 5 adsorption sites on the clusters were calculated and listed in **Table 4-2**.

It is clearly noticeable that the ν(Pt-O) stretching frequency values in Ni@Pt cluster are generally higher than their counterparts in pure Pt cluster for all sites. The discrepancy is mainly caused by the influence of Ni atoms as previously explained by Jacob et al [103]. Apart from that, our work and theirs also share one common similarity which agrees that higher vibrational frequencies do not always proportionally correlated to higher oxygen adsorption energy or vice versa. Through careful analysis, there is a clear decreasing trend of frequency gap between edge-bridge and three-fold hollow sites as this tendency systematically obeys the successive order of Pt(335) > pure Pt > Ni@Pt as shown in **Table 4-2** (the right-most column). This phenomenon of narrowing frequency gap can be interpreted as an indication that the edge-bridge and three-fold hollow sites in the clusters are starting to impose similar Pt-O bonding strength due to geometry and alloying effects.

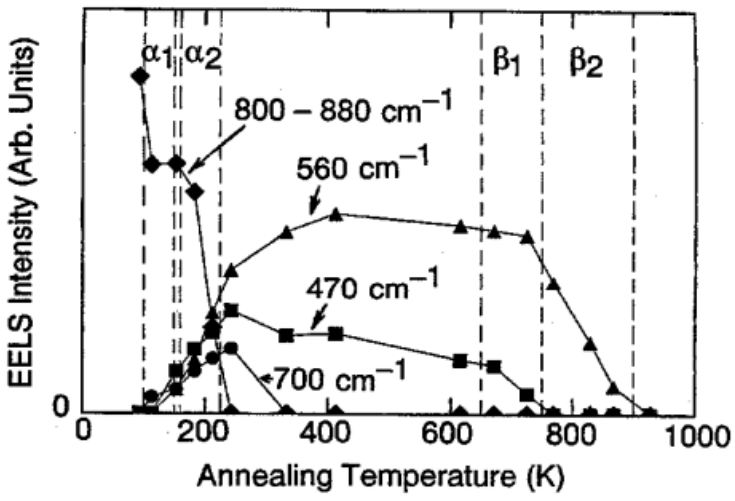

Figure 4-3 Intensities of the peaks of HREELS spectra measurement of oxygen on Pt(335), after heating a saturation coverage (at 90 K) to various temperatures [104]. α_1 (β_1) and α_2 (β_2) symbols are correspond to desorbed molecular (atomic) oxygen from terrace and step sites, respectively.

The oxygen on vertex sites is particularly interesting because it gains the highest ν(Pt-O) stretching frequencies above 700 cm^{-1} as compared with other sites. Previously, oxygen species with vibrational frequency values around 700 cm^{-1} had been observed by McCellan et al [102] and Wang et al [104] on Pt(321) and Pt(335) surfaces, respectively. Both authors concurred that the values emerge from metastable oxygen species at step sites. However, there was a disagreement between them whether the oxygen species that produce values near 700 cm^{-1} are in atomic or molecular state. Judging from their description (see **Figure 4-3** of Wang's work), we argue that the metastable oxygen species might have located at transition state (TS) because oxygen species at that state could undergo recombination to revert back to its molecular state or completely transforms itself into independent oxygen atoms. To prove our preconception, we have provided O-O stretching frequency values at TS in small Pt_4 and Pt_{10} clusters [105] as additional data for comparative analysis. The O-O bond distances in Pt_4 and Pt_{10} clusters at TS are subsequently 1.78 Å and 2.2 Å. These bond lengths dismiss the conjecture that refers the 700 cm^{-1} to the O-O stretching frequency at *peroxo* state since the O-O bond length at that state is around 1.42-1.43 Å [68]. In corresponding to oxygen atom on vertex A and vertex B sites, the situation can be interpreted as the oxygen atom is at metastable state which could later relocate onto more preferable sites such as bridge or hcp-like site if the conditions are permitted. Moreover, based on the data that presented in **Table 4-3**, the adsorption sites that could deliver Pt-O bond distances close to the experimental value [88] are only bridge, hcp-like, and fcc-like sites. This proves that adsorbed oxygen atom in real experimental conditions is less likely to occupy vertex sites for long periods of time. In summary, the global trend of Pt-O bonding strength in the clusters accommodates the following successive order of bridge (or hcp-like) > fcc-like > vertex A > vertex B.

Table 4-3 Average Pt-O bond length energies in reconstructed core-shell Ni@Pt and pure Pt clusters. The unit is given in Å.

Site	Ni@Pt	Pure Pt
Vertex A	1.77	1.80
Bridge	1.95	1.96
hcp-like	2.05	2.06
Vertex B	1.81	1.82
fcc-like	2.07	2.07
C-01	2.03	1.79[a]
	1.92	1.85[a]
C-02	1.95	1.96
	1.95	1.96
C-03	2.09	2.08
	2.08	2.09
C-04	1.78[b]	1.79[b]
	1.95	1.96
EXAFS [88]	N/A	2.00

oxygen atom that adsorbed on unstable structure[a] and vertex A site[b]

4.5 Cluster reconstruction in one-atom oxygen case

G.A. Somorjai and coworkers [106–108] reported that surface reconstruction could occur during chemical processes. In those studies, they proposed that surface metals are not completely rigid but instead have certain levels of flexibility and can undergo surface deformation where the surface of nano-structured cluster is considered to be the most flexible one. Xu et al [16] later confirmed the prediction of experimental studies above by showing that small Pt clusters could undergo major structural change at high oxygen coverage. In relation to our work, we studied cluster reconstruction that deviates Pt-Pt bond lengths in core-shell Ni@Pt and pure Pt clusters gives similar indicative trends that can be unambiguously compared to the reported works of spectroscopy measurements.

With the advent of new technical methods in XRD and XAFS experiments [87,88,109], it is now becomes possible to monitor *real-time* surface reconstruction on Pt nanoparticles when they are interacting with oxygen. In those experimental studies, Allen et al [87] (**Figure 4-4**) and Imai et al [88] (**Figure 4-5**) demonstrate how the amplitude of first nearest neighbor (1NN) Pt-Pt bond distribution that plotted in Fourier transform (FT) graph of EXAFS is decreasing while at the same time another amplitude that refers to Pt-O bonds is gradually increasing as the oxidation time passes. Most widely-accepted interpretation of this phenomenon suggests that the decreasing amplitude of 1NN Pt-Pt bond distance is caused by some of Pt-Pt bonds are elongating with few of them being contracted during Pt-O bonds formation. In similar way, we can also elaborate surface reconstruction or more

precisely cluster reconstruction by analyzing 1NN distribution pattern using a simple model. The model was applied on the clusters by simply comparing the lengths of all bonds in the clusters before and after oxygen adsorption takes place as given in **Figures 4-6** and **4-7**. The figures explicitly display the total sum of 1NN shell Pt-Pt bonds at certain bond length range. For Ni@Pt (pure Pt) cluster case, the two green (red) high-intense peaks that assigned by A-B and B-B labels represent shell Pt-Pt bonds, while the background black line denotes the total sum of 1NN shell Pt-Pt bonds and the remaining interacting bonds in the clusters. The single black peak that located between them denotes the bonds that constructed by core and shell atoms (a_2,a_3), and the remaining peaks on the left side of A-B peak are contribution from the core atoms (a_0,a_1). Based on qualitative comparison, the double peaks of 1NN Pt-Pt bond distribution that plotted in **Figures 4-6** and **4-7** may look contrast to single Gaussian-like peak at 2.77 Å which routinely observed in FT graph of EXAFS measurement. This distinct discrepancy could stem from many factors such as geometric structure of Pt nanoparticles [90,110]. This can be explained as most of 1NN Pt-Pt bond distribution plots that reported in EXAFS measurement are not generated from single homogeneous structure of Pt nanoparticles but instead they are resulted from numerous non-uniform structures despite the average size of those Pt nanoparticles is relatively similar. However, the most reasonable reason that causes this striking discrepancy is size effect. Yevick and Frenkel [111] have demonstrated that the 1NN radial distribution function of Au cluster composed of 923 atoms (3.4 nm size) has continuous-like distribution pattern as opposed to the one consisting of 147 atoms (1.7 nm size) which acquires discrete-like distribution pattern. On the other hand, surface-induced strain effect that may exerted by Al_2O_3 surface on Pt-Pt bonds due to lattice mismatch imposes no significant influence on 1 nm Pt nanoparticles as reported by Nagai et al [112].

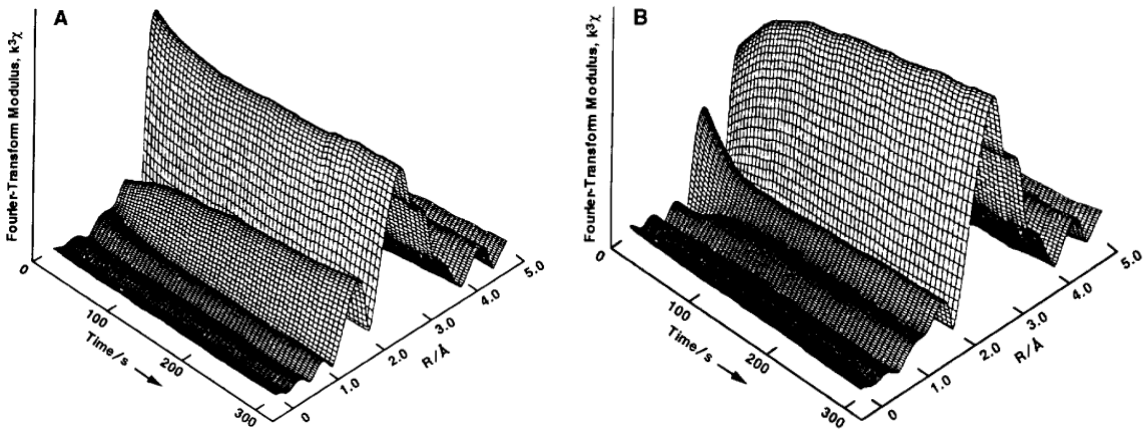

Figure 4-4 Fourier transform moduli of the Pt EXAFS (k = 2.2-9.7 $Å^{-1}$) acquired during (A) the oxidation and (B) the reduction of Pt catalyst as a function of time. The peak at 2.24 Å corresponds to the first shell of Pt nearest neighbors at 2.76 Å. The peak at 1.50 Å is a combination of the side-lobe from the Pt shell and a shell of O nearest neighbors at 2.01 Å [87].

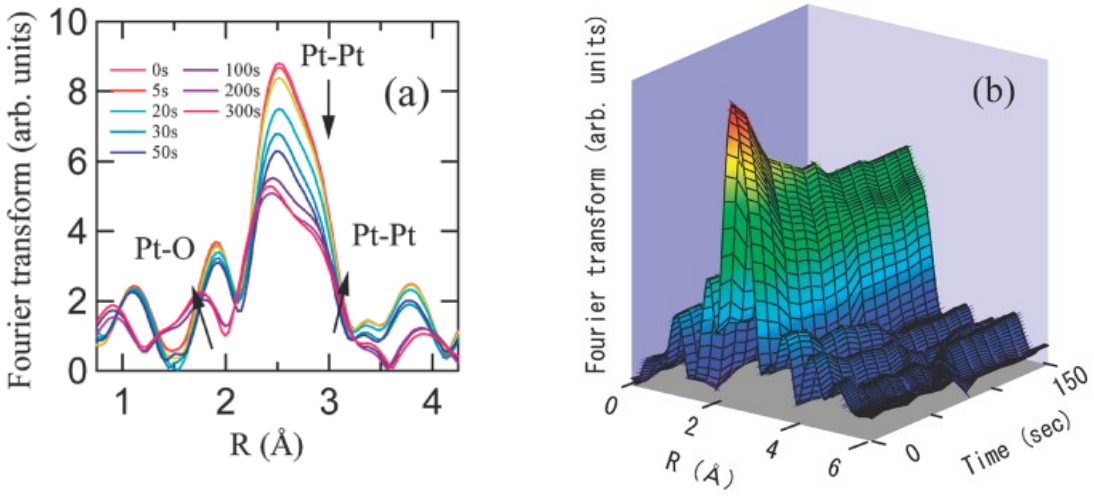

Figure 4-5 Time variations in k^3-weighted Fourier transforms of Pt-L_3 EXAFS (a and b) during potential step oxidation at 1.4 V. (1) Amplitude of first nearest neighbor Pt-Pt bonds decrease, and in turn (2) amplitude for Pt-O and (3) longer Pt-Pt bonds increase [88].

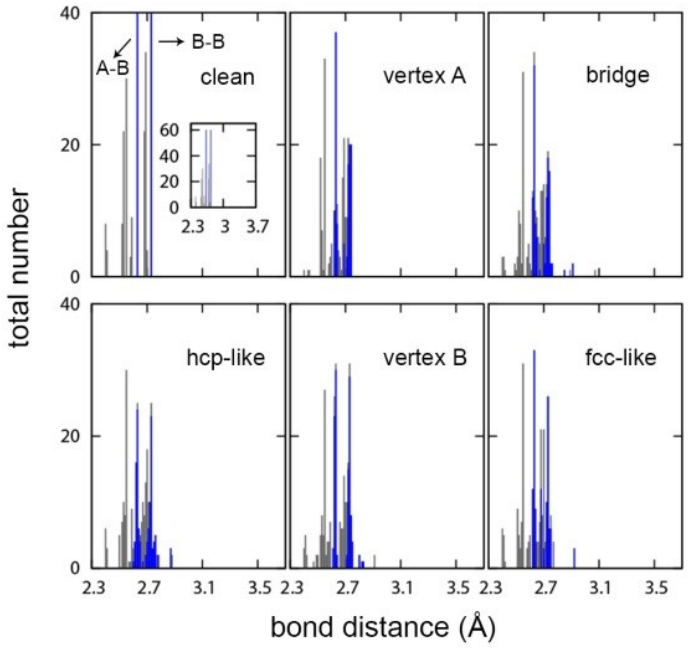

Figure 4-6 First nearest neighbor (1NN) Pt-Pt bond distribution in core-shell Ni@Pt cluster for one-atom oxygen case. Dark grey and blue bars correspond to whole cluster and surface (shell) Pt atoms, respectively. The inset shows the zooming out of "clean" 1NN Pt-Pt bond distribution.

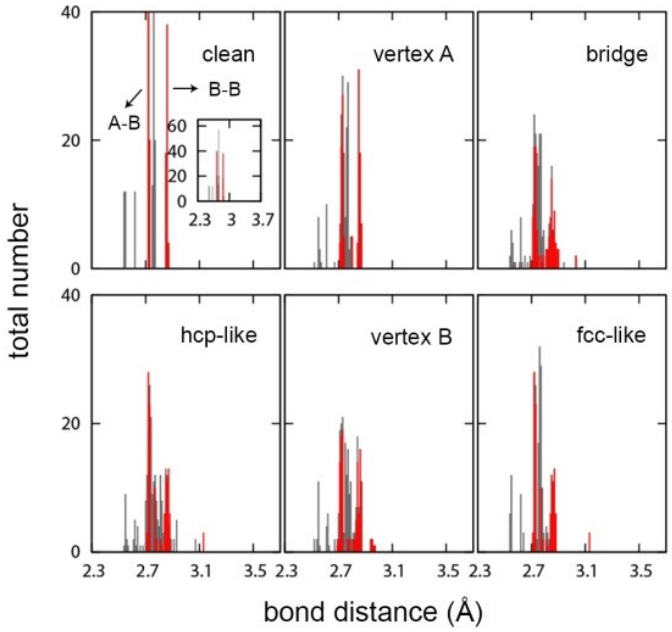

Figure 4-7 First nearest neighbor (1NN) Pt-Pt bond distribution in pure Pt cluster for one-atom oxygen case. Dark grey and red bars correspond to whole cluster and surface (shell) Pt atoms, respectively. The inset shows the zooming out of "clean" 1NN Pt-Pt bond distribution.

When oxygen adsorbed and induced moderate cluster reconstruction, the intensity of those A-B and B-B peaks are reduced since some of Pt-Pt bonds are slightly elongated and contracted by average value of 0.01 Å. This trivial bond length change produces new 1NN distribution patterns and these new patterns are also distinguishable from one to other adsorption sites on the same or different clusters. From overall observation, there is no shell Pt-Pt bonds elongation in Ni@Pt cluster that exceeds 3.1 Å. Similar result also obtained from pure Pt case except those from hcp-like and fcc-like sites where the low-intense peaks above the value 3.1 Å are presumably coming from stretched (B-B)-assigned Pt-Pt bonds. Here, we assume that the coordination number (CN) of Pt atoms remains unchanged unless stated otherwise, for instance, if the bonds are found to be broken. These results prove that the shell Pt-Pt bonds in 1 nm Ni@Pt and pure Pt clusters are not as rigid as we have thought before despite the clusters can still robustly maintain their former structure.

4.6 Cluster reconstruction in two-atom oxygen case

In order to verify whether 1NN model is sufficient to discern the distribution patterns of 1NN Pt-Pt bonds between those induced by one or more oxygen atoms, we have further extended the investigation on two oxygen atoms case where the atoms are configured to resemble oxygen atoms that dissociated from molecular state. This atom rearrangement was intentionally reproduced to allow us to examine oxygen-induced reconstruction effect on both clusters that previously has been neglected in previous studies. As depicted in **Figure 4-8**, four Pt-O bonds configurations are proposed and all of their structures have been fully relaxed.

Among those four configurations, C-01 of Ni@Pt cluster clarified our early prediction that vertex A site is harboring a metastable oxygen atom where the atom that initially resided on vertex A was displaced to hcp-like site after the structure was optimized. The displacement is more likely to occur as an effort to minimize repulsive lateral interaction between the neighboring oxygen atoms. On the other hand, the oxygen atoms in C-01 of pure Pt cluster remain adhere to their initial positions, however unlike Ni@Pt case, the formation of Pt-O bonds has inflicting bond breaking process as indicated by three

broken bonds (blue lines) in **Figure 4-8**. For validation, calculations of C-01 of pure Pt cluster were carried out three times using different force criteria and all led to the same result. The standard DFT-based structure optimization is deemed to offer no guaranteed success in finding the stable structure. Such case should be more appropriate to be tackled by molecular dynamics treatment which has higher success rate, which unfortunately, such work is computationally time-consuming and does not serve the current objectives of this study. Hence, the current geometric structure of C-01 of pure Pt cluster is a metastable structure. Nevertheless, the result has demonstrated that core-shell Ni@Pt cluster is relatively more stable than pure Pt cluster. In addition, the oxygen adsorption energies of pure Pt clusters are also well comparable to the experimental work of Parker et al [113] (see **Table 4-4**) where at zero oxygen coverage the oxygen desorption energy of those dissociated oxygen atoms was found to be at 51 kcal/mol or 2.21 eV. This good agreement between theoretical and experimental data fortifies the notion that dissociated oxygen atoms in small Pt nanoparticles are more preferably to choose edge-bridge sites over other sites.

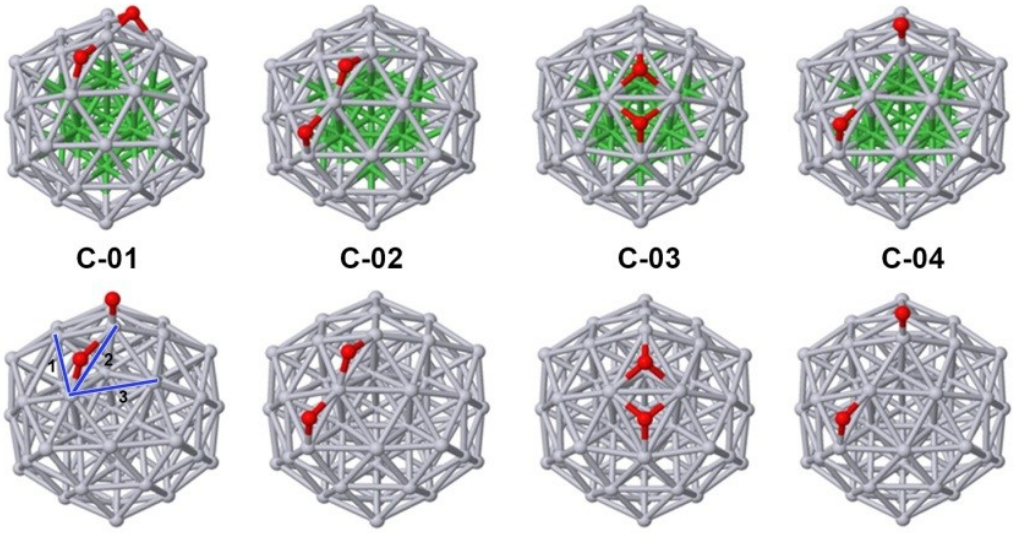

Figure 4-8 Geometric configurations of two adsorbed oxygen atoms in reconstructed core-shell Ni@Pt and pure Pt clusters.

Table 4-4 Oxygen adsorption energies in Ni@Pt and pure Pt clusters for two-atom oxygen case

	C-01	C-02	C-03	C-04
Ni@Pt	-2.45	-2.20	-1.30	-1.80
Pure Pt	N/A*	-2.29	-1.90	-2.18

*Not avalaible

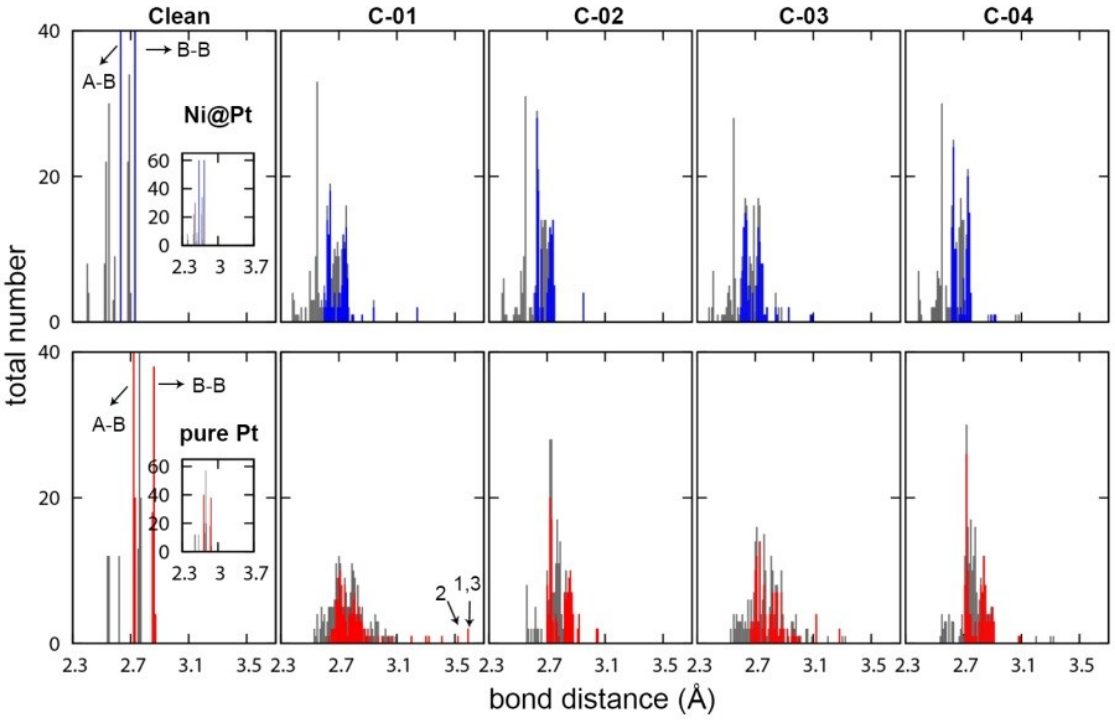

Figure 4-9 First nearest neighbor (1NN) Pt-Pt bond distribution in core-shell Ni@Pt (top panels) and pure Pt clusters (bottom panels) for two-atom oxygen case. For details, please refer to **Figures 4-6** and **4-7**.

Figure 4-9 shows 1NN Pt-Pt bond distributions in two-atom oxygen case. In comparison to one-atom oxygen case, it is obvious that none of these 1NN distribution patterns resemble those of one-atom oxygen case since the intensity of their A-B and B-B peaks is more deeply suppressed than the former case. The sole reason of differences between these two cases is caused by recursive effect of Pt-Pt bond length deviation as adding another oxygen atom onto the clusters surface will once more perpetuate cluster reconstruction. In particular case, the reconstruction could also lead to broken Pt-Pt bonds such the one found in C-01 of pure Pt cluster that followed by three prevalent yet unique

traits on its 1NN Pt-Pt distribution pattern. First, the intensity of A-B and B-B peaks are strongly weakened as compared to the others. Second, there are more new emerging peaks at Pt-Pt bond distance range of 3.1 - 3.5 Å while other configurations only have few of them. The last one is that beyond the limit value of 3.5 Å there are still other three peaks observed, one at 3.52 Å (number 2) and the remaining two peaks at 3.59 Å (numbers 1 and 3). These three peaks are representing those three broken Pt-Pt bonds of C-01 of pure Pt cluster that portrayed in **Figure 4-8**. In addition, these peaks are located more closer to the vicinity of second nearest neighbor (2NN) Pt-Pt bond distances of 3.92 Å [114] Hence, we argue that these three peaks are no longer belong to the group of 1NN Pt-Pt bond distribution and convincingly convey them as broken Pt-Pt bonds. Accordingly, the coordination number of those Pt atoms is also reduced.

While there is a contrast difference of 1NN Pt-Pt bond distribution pattern between each adsorption site in one-atom and two-atom adsorbed oxygen cases, the average Pt-O bond length that observed in both cases does not vary so much. The values are relatively close to the experimental value of 2 Å as shown in **Table 4-3** with exceptions those Pt-O bonds that established on vertex sites or C-01 of pure Pt cluster are slightly deviated. This proves that the length of Pt-O bonds is independent from the cluster size and alloying effects which agrees well with previous works [90,103,110]. Based on thorough analysis above, Pt-Pt bonds in pure Pt cluster are more prone to be distorted under the presence of oxygen rather than those contracted Pt-Pt bonds in core-shell Ni@Pt cluster, and this trait becomes more prevalent in two-atom oxygen case. Lastly, the general result shows that adsorbed oxygen is not only locally induced atom rearrangement near the surrounding adsorption site but also globally affected the connecting bonds of whole cluster atoms including the core atoms. This phenomenon is not limited to the oxidized Ni@Pt and pure Pt clusters only, similar observation had also been reported in oxidized Na_{55} cluster [115].

4.7 Bader analysis of oxidized Ni@Pt and pure Pt clusters

In this section, we discuss the bonding nature between the clusters and oxygen by using Bader charge analysis method [116,117]. For one-atom oxygen case, unexpectedly, Bader charge analysis reveals that there is a general trend that indicates an increasing of charge transfer from Pt to O is proportionally equal to a steady increase of oxygen

adsorption energy as observed in both clusters (see **Table 4-5**) with an exception in fcc-like site in Ni@Pt cluster where the trend is reversed. As additional information, the amount of charge transfer that received by oxygen on each adsorption site could also be used to identify the bonding character of Pt-O bonds formation. For instance, the charge transfer from Pt to O in vertex sites in pure Pt cluster is only about half of that in bulk PtO [16,118], indicating more covalent character instead of ionic character. However, the level of ionicity of Pt-O bonds approaches the bulk level as oxygen becomes strongly adsorbed on the clusters although the highest amount of charge transfer is still far below the value of bulk PtO. In overall, the ionicity level of Pt-O bonds on pure Pt cluster varies and greatly depends on which adsorption site the oxygen is adsorbed. For the dissociated (two-atom) oxygen case, Pt-O bonds configuration on the clusters has strong similarity with Pt-O oxide structure of Pt_xO_{2x} cluster in term of the amount of total charge transfer. Based on the data provided in **Table 4-6**, the amount of charge transfer are twice of those in single atom cases. Another distinctive trait of Pt-O bonds in dissociated oxygen atoms case is that the increment of charge transfer as the function of oxygen adsorption energy is nearly constant with the highest value is similar with the value (-0.63*e*) found in the smallest size of Pt_xO_{2x} cluster (PtO_2) [16]. Hence, it appears that most of Pt-O bonds are becoming more covalent with respect to those bonds in either bulk β-PtO_2 or even bulk PtO when there is more than one adsorbed oxygen atom residing the clusters. This result may explain previous experimental work on Pt/Al_2O_3 [119] where the surface oxide species that forms on Pt nanoparticles with diameters < 1.3 nm is PtO_2. In addition, C-03 is the only configuration that does not follow the trend and further investigation is needed in order to address this matter.

In similar way, the explanation above can also be used to rationalize the same trend that observed on Ni@Pt cluster. Although no study has ever been conducted on bulk NiPt oxide due to such system might be unknown or non-existence, bulks PtO and β-PtO_2 can still be used as reference to evaluate the ionicity level of Pt-O bonds on Ni@Pt cluster. The reason is that the oxide surface is still consisting of Pt-O bonds while there is no significant difference on the charge transfer between the one that transferred from Ni@Pt and pure Pt clusters. Therefore, the ionicity level of Pt-O bonds of oxidized Ni@Pt and pure Pt clusters is more or less the same regardless profound difference of their oxygen adsorption energy.

Another consequence is that one would always be able to detect the presence of oxide forms such as PtO and PtO_2 on the surface of Ni@Pt and pure Pt clusters where similar observation on other bimetallic Pt-M catalyst (where M =Au, Pd, Ru, Fe) has been reported by XPS spectra results [120].

Table 4-5 Bader atomic charges for one-atom oxygen case

cluster	adsorption site	charge (*e*) on cluster	charge (*e*) on O atom	adsorption energy (eV)
Ni@Pt	vertex B	+0.45	-0.45	-3.45
	vertex A	+0.58	-0.58	-4.06
	bridge	+0.63	-0.63	-4.51
	fcc-like	+0.71	-0.71	-4.22
	hcp-like	+0.76	-0.76	-4.51
pure Pt	vertex B	+0.48	-0.48	-3.76
	vertex A	+0.47	-0.47	-4.27
	bridge	+0.63	-0.63	-4.55
	fcc-like	+0.68	-0.68	-4.55
	hcp-like	+0.73	-0.73	-4.61
PtO		+0.48[a]	-0.48[a]	
Bulk PtO		+0.96[a]	-0.96[a]	
		+0.86[b]	-0.86[b]	

See references [16][a] and [118][b]

Table 4-6 Bader atomic charges for two-atom oxygen case

cluster	adsorption site	charge (*e*) on cluster	charge (*e*)* on O atom	adsorption energy (eV)
Ni@Pt	C-04	+1.18	-0.59	-1.8
	C-02	+1.24	-0.62	-2.2
	C-03	+1.3	-0.65	-1.3
	C-01	+1.37	-0.69	-2.45
pure Pt	C-04	+1.2	-0.6	-2.18
	C-02	+1.24	-0.62	-2.29
	C-03	+1.32	-0.66	-1.9
PtO_2		+1.27[a]	-0.63[a]	
Bulk β-PtO_2		+1.70[a]	-0.85[a]	
		+1.62[b]	-0.81[b]	

*For the sake of clarity, the average charge of two O atoms is reported. C-01 in pure Pt is excluded from the list since its oxygen adsorption energy could not be obtained.
See references [16][a] and [118][b]

4.8 Ni-Pt bond weakening vs Pt-Pt bond strengthening

In order to understand the mechanism of adsorbed oxygen on the clusters in disrupting the bonding at core/shell interface, schematics of three selected adsorption sites that obtained by slicing through atoms with A-c-B-c-A labels (see **Figure 4-2(a)**) are presented in **Figure 4-10(a-c)**. For vertex A and bridge sites case, **A**-designated shell Pt and **c**-designated core Ni (or Pt) atoms are distinguished by assigning them number to indicate which Pt and/or Ni atom(s) that involved in the bond weakening/strengthening process at core/shell interface.

For vertex A site case in pure Pt cluster (two upper panels on the left side of **Figure 4-11**), after oxygen adsorbed, strong 2p-5d hybridization between oxygen and shell Pt($\mathbf{A_1}$) atoms generates two distinct sequential peaks of bonding and anti-bonding regions. Surprisingly, the 5d electrons of core Pt($\mathbf{c_1}$) atom are also redistributed and occupied the same energy levels of bonding and anti-bonding regions that adopted by 5d electrons of Pt($\mathbf{A_1}$) atom. Since the 5d electrons of both Pt atoms that make contribution to constructive bonding of Pt($\mathbf{c_1}$)-Pt($\mathbf{A_1}$) bond are shifted to lower energy level while the electrons that build anti-bonding interaction are displaced above the Fermi level, it can be translated that Pt($\mathbf{c_1}$)-Pt($\mathbf{A_1}$) bonding strength has been increased, hence, the 5d-5d hybridization of this Pt(core)-Pt(shell) bond has generated more attractive-dominated bonding characteristic under oxygen presence.

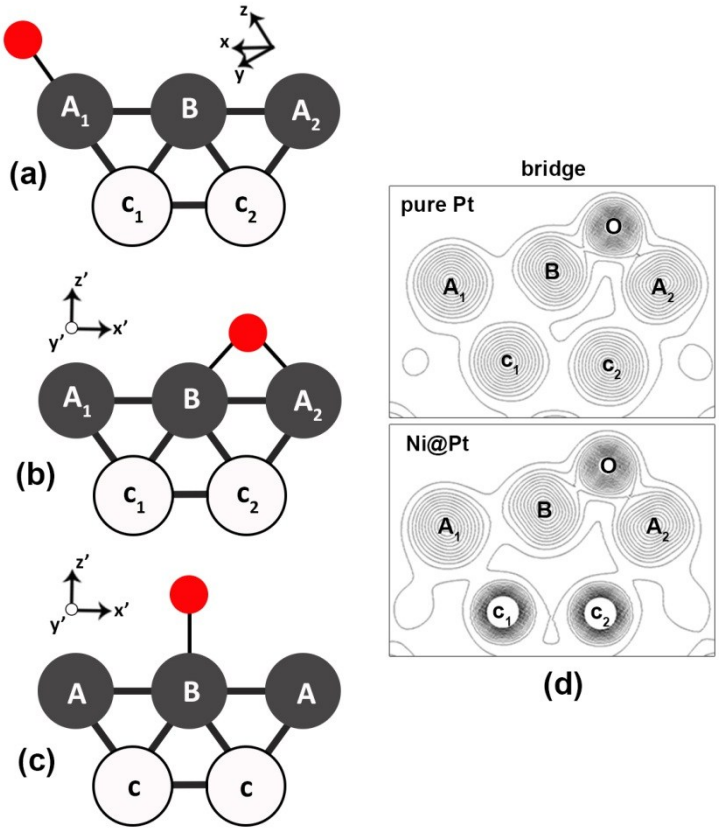

Figure 4-10 Schematics of three selected adsorption sites: (a) vertex A, (b) bridge, and (c) vertex B which obtained by slicing through atoms with A-c-B-c-A labels. Red, black, and white spheres are representing oxygen, shell Pt, and core atoms, respectively. The y-axis in bridge and vertex B sites is pointing inward. Charge density distribution in Ni@Pt and pure Pt clusters for bridge site case **(d)** is gained using isosurface interval 4.5 x 10^{-3} *e*/Å^3.

In Ni@Pt cluster case (two bottom panels on the left side of **Figure 4-11**), the 2p-5d hybridization provides electron distribution profile that nearly the same with the one exhibited in pure Pt cluster. However, the 3d electrons of Ni(**c_1**) atom are unexpectedly shifting into interval energy region [-3.3, -0.35]. Since the majority distribution of Ni(**c_1**)-3d and Pt(**A_1**)-5d electrons in post-oxygen adsorption state is no longer stay at the same energy range, it can be interpreted that Ni(**c_1**)-Pt(**A_1**) bond has been weakened. Therefore, the 3d-5d hybridization of Ni(core)-Pt(shell) bond has become more repulsive after Pt-O bond is formed. Partial charge density distribution plots in **Figure 4-12** further rationalize this bond weakening process in Ni@Pt cluster as follows. The weakening bonding strength of Ni(**c_1**)-Pt(**A_1**) bond would be compensated by increasing bonding strength of Ni(**c_1**)-

Ni($\mathbf{c_3}$) bond possibly due to electron transfer from Ni($\mathbf{c_3}$) to Ni($\mathbf{c_1}$) atom as clarified by the plots at energy region [-3.3, -2.3]. But some amount of these electrons would also contribute to the increasing repulsive (anti-bonding) interaction between these atoms as emphasized by charge density plots at [-2.3, -0.35].

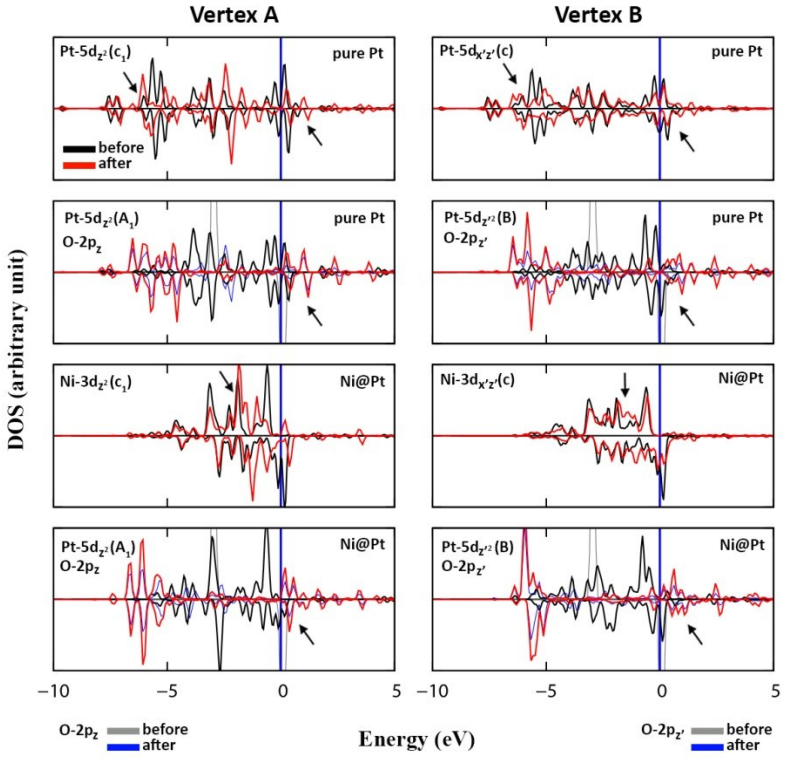

Figure 4-11 Projected density of states (PDOS) describe bonding interactions between shell Pt and core Pt (or Ni) atoms in vertex A (left) and B (right) sites. Solid black (gray) and red (blue) lines correspond to the conditions of Pt 5d and Ni 3d states (O 2p states) before and after oxygen adsorption take place. The Fermi level is taken at zero energy level. The arrows serve as eye guidance for 3d and 5d electrons final displacement positions after oxygen is adsorbed.

For vertex B site case, different cartesian coordinate system (x', y', z') is used as indicated in **Figures. 4-10(c)** and **4-12**. When oxygen is adsorbed on the clusters, the Pt(**c**)-5d electrons of pure Pt cluster would undergo similar displacement that experienced by Pt($\mathbf{c_1}$)-5d electrons in vertex A case. In similar way, some amount of Ni(**c**)-3d electrons of Ni@Pt cluster are also shifted to the interval energy region [-3.3, -0.35] and breaking Ni(**c**)-Pt(**B**) bonds as clearly seen in charge density plots in **Figure 4-12**. The event of broken Ni(**c**)-Pt(**B**) bonds in Ni@Pt cluster is also subsequently followed by expanding

contour area of charge density (shaded region) that envelops Ni(**c**) and Ni(**c_3**) atoms. Through depiction of partial charge density plot in **Figure 4-12** at energy range [-2.3,-0.35], it is found that Ni(**c**)-Ni(**c**) bond has been strengthened instead of Ni(**c**)-Ni(**c_3**) bonds since there is a rise of charge density accumulation in the midpoint region of Ni(**c**)-Ni(**c**) bond axis after oxygen adsorption occurred.

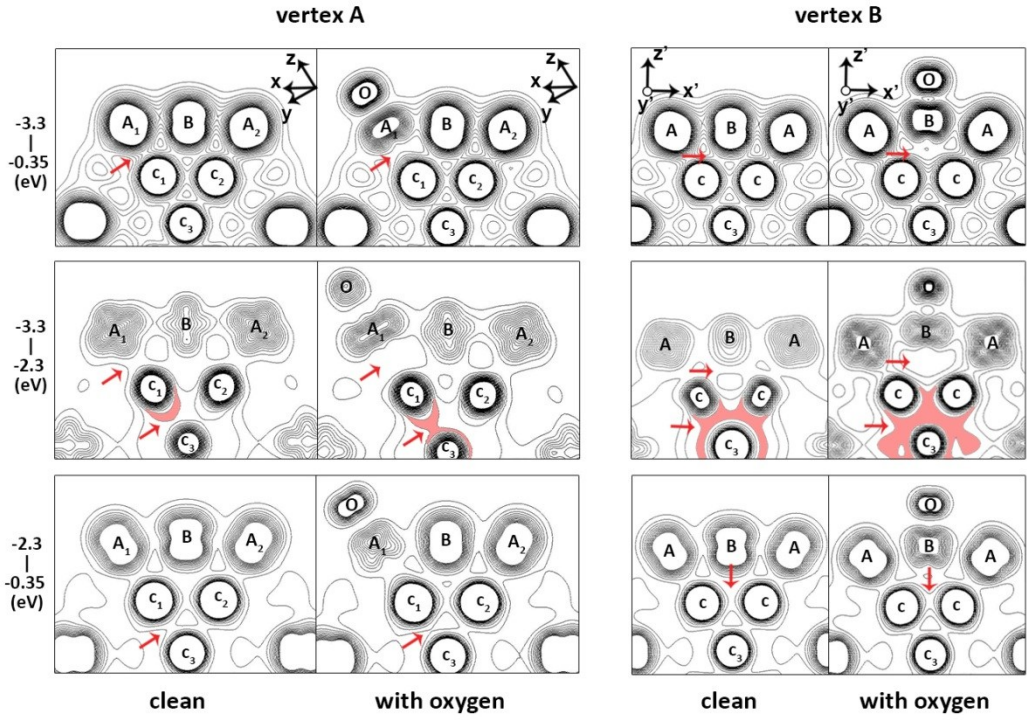

Figure 4-12 Contours of partial charge density distribution in Ni@Pt cluster for the case of vertex A and vertex B sites. The partial charge density plots at interval energies [-3.3, -0.35] and [-3.3, -2.3] are drawn using isosurface interval 4.5 x 10^{-3} e/Å^3, while the plots at [-2.3, -0.35] is obtained using isosurface interval 7 x 10^{-3} e/Å^3 for better clarity and contrast.

4.9 Bonding stability between Ni(core)-Pt(shell) and Pt(core)-Pt(shell) bonds

Finally, the bonding at core/shell interface in bridge site would be evaluated to conclude the investigation on the stability of Ni-Pt bonds in Ni@Pt cluster (see **Figure 4-10(d)**). In the bridge site, the charge density distribution of the atoms near the vicinity of core/shell interface is quite unique as it renders attractive and repulsive bonding characters concurrently following oxygen adsorption process. In pure Pt cluster, the attractive bonding

interaction at Pt(core)/Pt(shell) interface is represented only by Pt($\mathbf{c_1}$)-Pt(**B**) bond, while the repulsive ones are given by Pt($\mathbf{c_2}$)-Pt(**B**) and Pt($\mathbf{c_2}$)-Pt($\mathbf{A_2}$) bonds. With respect to equilibrium Pt(core)-Pt(shell) bond distances (without oxygen), their bond lengths are readjusted by -0.06 Å, 0.17 Å, and 0.04 Å, respectively. The contracted Pt($\mathbf{c_1}$)-Pt(**B**) bond (minus sign) is one of good indications that its bond has been strengthened. In Ni@Pt cluster case, all bonding interactions at Ni/Pt interface are deemed to impose repulsive (anti-bonding) interaction as demonstrated by Ni($\mathbf{c_1}$)-Pt(**B**), Ni($\mathbf{c_2}$)-Pt(**B**), and Ni($\mathbf{c_2}$)-Pt($\mathbf{A_2}$) bonds, and all of their bonds are being stretched by 0.21 Å, 0.38 Å, and 0.06 Å consecutively.

PDOS description in **Figure 4-13** reconfirmed the above statement by showing that core atoms Ni($\mathbf{c_1}$) and Ni($\mathbf{c_2}$) in Ni@Pt cluster emulate an increase of anti-bonding interaction after oxygen adsorbed, while in pure Pt cluster this trait can only be seen in Pt($\mathbf{c_2}$) atom. As additional information, Pt($\mathbf{c_2}$)-Pt($\mathbf{A_2}$) and Ni($\mathbf{c_2}$)-Pt($\mathbf{A_2}$) bonds are being noticed to have the shortest bond elongation values with respect to those of Pt($\mathbf{c_2}$)-Pt(**B**) and Ni($\mathbf{c_2}$)-Pt(**B**) bonds. The main reason is that the anti-bonding interaction in the former bonds occurs in similar atomic orbital (d_{xz}) while the one that built in the later bonds is resulted from different atomic orbitals (d_{xz} vs d_{z^2}), hence, their anti-bonding interaction becomes less effective.

Bond strengthening that occurs on Pt($\mathbf{c_1}$)-Pt(**B**) bond is similar to the case of Pt-Pt bond strengthening when oxygen atom is adsorbed on fcc site of Pt(111) surface, while bond weakening that happens on Pt($\mathbf{c_2}$)-Pt(**B**) and Pt($\mathbf{c_2}$)-Pt($\mathbf{A_2}$) bonds is equivalent to the case of Pt-Pt bond weakening that rendered by adsorbed oxygen atom on hcp site. This bond strengthening and weakening phenomenon has been called d-electron frustration by Feibelman [121]. This proves that Pt-Pt bonds in pure Pt cluster and Pt(111) surface react in similar way towards oxygen. However, Ni-Pt bonds in Ni@Pt cluster do not accommodate this model where adsorbed oxygen atom on any site would always cause Ni-Pt bond weakening.

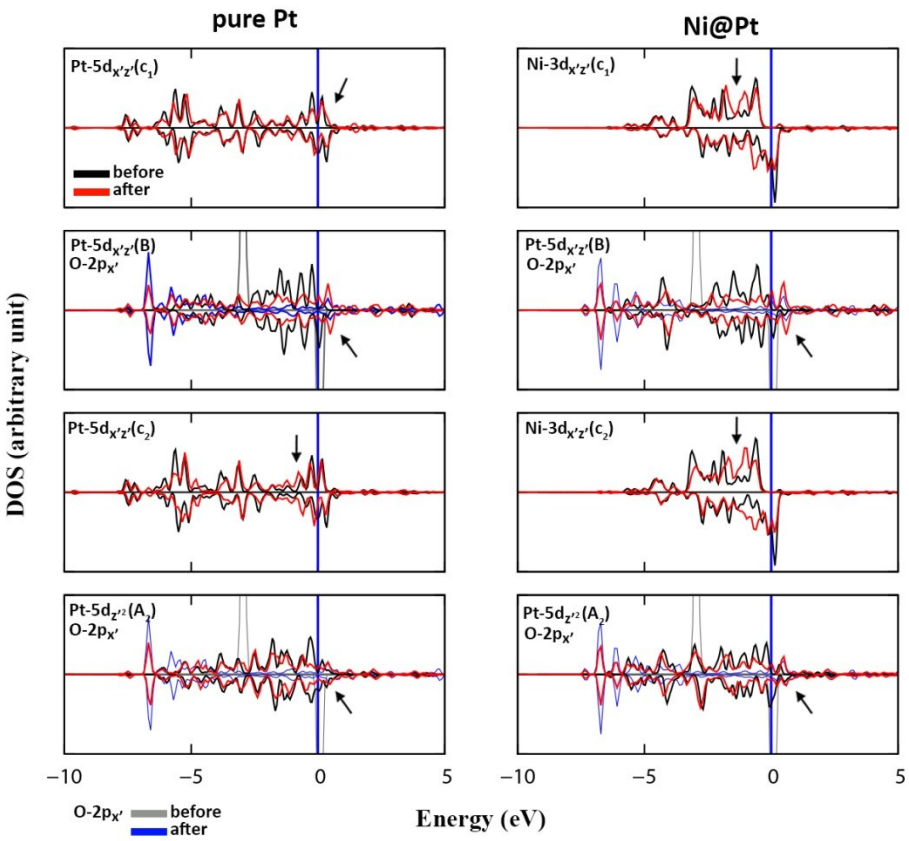

Figure 4-13 Projected density of states (PDOS) of bonding interactions between shell Pt and core Pt (or Ni) atoms in bridge site case. For details, please see caption of Figure 4-11.

Nonetheless, the analogy of this model can be helpful to explain the main reason why Ni(**c$_2$**)-Pt(**B**) bond could be stretched more than twice of bond elongation that experienced by Pt(**c$_2$**)-Pt(**B**) bond (0.38 Å against 0.17 Å). Because of oxygen adsorption, charge transfer from Pt(**B**) to oxygen atom leading to increasing repulsive force between these two atoms. To prevent this, excessive charge of Pt(**B**)-5d states atom along Pt(**B**)-O bond axis must be allocated to somewhere else like Ni(**c$_2$**) or Pt(**c$_2$**) atom. Since most of unoccupied Pt(**c$_2$**)-5d states are anti-bonding, charge donation from Pt(**B**) is equivalent to bond weakening. For Ni(**c$_2$**) atom case, due to Pt atom has greater electronegativity than Ni atom, it is unlikely charge donation from Pt(**B**) to Ni(**c$_2$**) atom would occur. Hence, the Pt(**B**) atom only option is to move away as far as possible from Ni(**c$_2$**) atom. The increasing of anti-bonding profile that perpetuated by Ni(**c$_2$**)-3d$_{xz}$ states (see **Figure 4-13**) is presumed because of Ni(**c$_2$**) atom interacts with another nearest neighbor Ni atom likewise the case of

Ni($\mathbf{c_1}$)-Pt($\mathbf{A_1}$) bond in vertex A site. In summary, the stability of Ni(core)-Pt(shell) bonds in core-shell Ni@Pt cluster is more easily disrupted by oxygen

4.10 Summary

In summary, we have examined the core-shell structure of Ni@Pt and its corresponding pure Pt cluster to investigate the preferable adsorption sites for oxygen atoms. In general, the oxygen adsorption energy is mainly governed by (1) atomic configuration of Pt-O bonds, (2) alloying and (3) cluster reconstruction effects. Based on oxygen adsorption energy and ν(Pt-O) stretching frequency calculations and comparison with available experimental data, the global trend of Pt-O bonding strength in the clusters is more likely to follow successive order of bridge (and/or hcp-like) > fcc-like > vertex A > vertex B where the vertex sites are presumed to harbor "metastable" oxygen atoms. In overall, core-shell Ni@Pt cluster is able to reduce Pt-O bonding strength despite on bridge site case the adsorption energy is relatively similar to the one in pure Pt cluster.

We also have shown that the 1NN model can qualitatively be used to compare the changes in 1NN Pt-Pt bond distribution patterns with the one of Fourier transformed of EXAFS data. Although there are some noticeable differences between these two types of data because of several factors, the general trend of our results and those of experimental works are vividly alike where the amplitude of 1NN Pt-Pt bond distribution of surface atoms would decrease as oxygen absorbed on the clusters. Moreover, oxygen-induced cluster reconstruction affects both shell Pt-Pt bond lengths near the proximity of the adsorption site and globally the lengths of all interacting bonds that are located at great distance from the position of Pt-O bonds formation. In addition, the average length of Pt-O bonds in the cluster is similar with the experimental values. In term of structural robustness, the role of Ni core atoms in core-shell Ni@Pt is to prevent bond breaking process on shell Pt-Pt bonds. Finally, based on Bader charge analysis, the majority bonding character of Pt-O bonds in the clusters is covalent. However, more ionic characters might occur as Pt-O bonding strengths are increased.

The influence of Pt-O bonds formation involving surface reconstruction on the bonding interaction at core/shell (Ni/Pt) interface has been investigated. The result shows

that 5d-5d hybridization of Pt(core)-Pt(shell) bonds in pure Pt cluster in the presence of oxygen can turn into more attractive or repulsive bonding character depending on the structural configuration of Pt-O bonds. In Ni@Pt cluster, the 3d-5d hybridization of Ni(core)-Pt(shell) bonds under oxygen presence would always developed into repulsive bonding character, hence, weakening Ni(core)-Pt(shell) bonding strength. This study further proves that Ni(core)-Pt(shell) and Pt(core)-Pt(shell) bonds act and response differently towards adsorbed oxygen atom.

Chapter 5
Conclusions

Elucidating a detailed mechanism how small Pt clusters interact with oxygen has become interest of many theoretical and experimental studies in the last few years to find out a fundamental rationalization of Pt-O bonding interaction that leads to oxygen poisoning in Pt/Al_2O_3. This thesis was aimed at figuring out a relationship between three inherent parameters (geometry, size, alloying) and reactivity of small Pt clusters at atomic scale. Density functional theory (DFT)-based study approach was used for the purpose of the investigation in this study.

In chapter 2, we characterized detailed geometry effect of small Pt clusters under isolated and supported conditions. It was found that two isomers of Pt_4 clusters that share similar atom number can possess different reactivity towards NO molecule. In addition, the geometric structure of Pt_4 cluster has significant contribution in determining the stability of bonding interaction at Pt_4/Al_2O_3 interface. This bonding strength difference between these two isomers of Pt_4 clusters at the interface can be explained as more Pt atoms at Pt_4/Al_2O_3 interface interact with Aluminum atoms on Al_2O_3 surface; it will reduce repulsive force that exerted on Pt-O bonds at the interface. In summary, isomer of Pt_4 clusters that has slightly weaker bonding interaction with NO molecule and strongly interacts with Al_2O_3 support such as tetrahedron-structured Pt_4 cluster is more attractive to be employed in DOC.

The study in chapter 3 underlines the importance of cluster reconstruction contribution in adjusting the energy barrier of oxygen dissociation process and how size of small Pt clusters (Pt_4 vs Pt_{10}) plays major role in determining oxygen adsorption energy. The study is divided into two main parts. The first part is to identify the underlying mechanism that initiates cluster reconstruction. The result shows that the weakening process of interstitial bonding orbital (IBO) that induced by adsorbed molecular oxygen is the main source that initially triggers cluster reconstruction. The second part of the study discusses how rigid Pt-Pt bonds in Pt clusters are more likely to induce energy barrier during O_2 dissociation process as compared to loose Pt-Pt bonds. This due to rigid Pt-Pt bonds tend to disrupt near-equilibrium of intramolecular forces between atoms, therefore,

increasing the net attractive or repulsive forces that directly contribute to the rising of energy barrier. On the other hand, loose Pt-Pt bonds can suppress this energy barrier by keep maintaining attractive and repulsive forces between atoms close to equilibrium through atom rearrangement.

The final chapter presents a preliminary study of core-shell Ni@Pt cluster that is being proposed as a prospective candidate for new DOC. Core-shell-typed structure Ni-Pt alloy was chosen to prevent oxygen from making direct contact with Ni atoms. The average bonding strength of Pt-O bonds on Ni@Pt cluster is weaker than the one in pure Pt cluster of similar size. Based on the numerical result and existing experimental data, the most-to-least preferable adsorption sites on the clusters follows successive order of bridge or hcp-like > fcc-like > vertex A > vertex B where the vertex sites are presumed to harbor "metastable" oxygen atoms. Furthermore, we introduced simple first nearest neighbor (1NN) analysis method to evaluate the change in 1NN Pt-Pt bond distribution pattern on the clusters as the result of surface reconstruction. Qualitatively, there is a good agreement between the calculated and experimental 1NN Pt-Pt bond distribution pattern data that indicates the amplitude of 1NN Pt-Pt bond distribution of surface atoms would decrease as oxygen absorbed on the clusters. Our result also shows that the pattern of 1NN Pt-Pt bond distribution is sensitive to the total number of oxygen that adsorbed on the surface of the clusters. In addition, it was found that the bonding interaction of Pt(core)-Pt(shell) bonds in pure Pt cluster can be switched in the presence of oxygen into more attractive- or repulsive-dominated bonding characters. In Ni@Pt cluster case, the bonding interaction of Ni(core)-Pt(shell) bonds under oxygen presence would always lead into repulsive-dominated bonding character, hence, weakening their Ni-Pt bonding strength.

Nonetheless, endorsing core-shell Ni@Pt cluster as substitution for small Pt clusters in DOC may serve as one of many possible solutions in lowering down the Pt loading while at the same time avoiding oxygen poisoning, and also encourage other follow-up research on DOC to investigate various combinations of alloyed transition metals for similar purpose. Lastly, the definite answer whether the core-shell would work or not when it is being implemented in DOC could only be given after experimental works in near future have finished making the validation of this study.

References

[1] J. Lewtas, *Mutat. Res.* 636 (2007) 95–133.

[2] http://www.utilitycontractoronline.com/index/siteb

[3] L. Olsson, H. Persson, E. Fridell, M. Skoglundh, and B. Andersson, *J. Phys. Chem. B* 105 (2001) 6895–6906.

[4] M. Crocoll, S. Kureti, and W. Weisweiler, *J. Catal.* 229 (2005) 480–489.

[5] R. J. Baxter and P. Hu, *J. Chem. Phys.* 116 (2002) 4379.

[6] K. Herbst, G. Mogensen, F. Huber, M. Østberg, and M. S. Skjøth-Rasmussen, *Catal. Today* 157 (2010) 297–302.

[7] B. Genc, "Where is platinum heading ?," *Third International Platinum Conference `Platinum in Transformation`* (2008) 401–406.

[8] S. Mulla, N. Chen, L. Cumaranatunge, G. Blau, D. Zemlyanov, W. Delgass, W. Epling, and F. Ribeiro, *J. Catal.* 241 (2006) 389–399.

[9] A. Boubnov, S. Dahl, E. Johnson, A. P. Molina, S. B. Simonsen, F. M. Cano, S. Helveg, L. J. Lemus-Yegres, and J.-D. Grunwaldt, *Appl. Catal. B Environ.* 126 (2012) 315–325 2012.

[10] M. N. Padilla-Serrano, F. J. Maldonado-Hódar, and C. Moreno-Castilla, *Appl. Catal. B Environ.* 61 (2005) 253–258.

[11] P. Briot, A. Auroux, D. Jones, and M. Primet, *Appl. Catal.* 59 (1990) 141–152.

[12] S. B. Simonsen, I. Chorkendorff, S. Dahl, M. Skoglundh, J. Shested, and S. Helveg, *Am. Chem. Soc.* 132 (2010) 7968–7975.

[13] R. Ishimoto, C. Jung, H. Tsuboi, M. Koyama, A. Endou, M. Kubo, C. A. Del Carpio, and A. Miyamoto, *Appl. Catal. A Gen.* 305 (2006) 64–69.

[14] Y. Xu, R. B. Getman, W. A. Shelton, and W. F. Schneider, *Phys. Chem. Chem. Phys.* 10 (2008) 6009–6018.

[15] A. Roudgar, M. Eikerling, and R. van Santen, *Phys. Chem. Chem. Phys.* 12 (2010) 614–620.

[16] Y. Xu, W. A. Shelton, and W. F. Schneider, *J. Phys. Chem. A* 110 (2006) 5839–5846.

[17] Y. Xu, W. A. Shelton, and W. F. Schneider, *J. Phys. Chem. B* 110 (2006) 16591–16599.

[18] S. R. de Miguel, I. M. J. Vilella, S. P. Maina, D. San José-Alonso, M. C. Román-Martínez, and M. J. Illán-Gómez, *Appl. Catal. A Gen.* 435–436 (2012) 10–18.

[19] M. García-Diéguez, E. Finocchio, M. Á. Larrubia, L. J. Alemany, and G. Busca, *J. Catal.* 274 (2010) 11–20.

[20] E. Örücü, F. Gökaliler, A. E. Aksoylu, and Z. I. Önsan, *Catal. Letters* 120 (2007) 198–203.

[21] B. S. Çağlayan, Z. İlsen Önsan, and A. E. Aksoylu, *Catal. Letters* 102 (2005) 63–67.

[22] J. Li, W. P. Tian, X. Wang, and L. Shi, *Chem. Eng. J.* 175 (2011) 417–422.

[23] F. Mittendorfer, A. Eichler, and J. Hafner, *Surf. Sci.* 433–435 (1999) 756–760.

[24] U. Achatz, C. Berg, S. Joos, B. S. Fox, M. K. Beyer, G. Niedner-schatteburg, and V. E. Bondybey, *Chem. Phys. Lett.* 320 (2000) 53–58.

[25] O. P. Balaj, I. Balteanu, T. T. J. Rossteuscher, M. K. Beyer, and V. E. Bondybey, *Angew. Chem. Int. Ed. Engl.* 43 (2004) 6519–22.

[26] G. Kummerlöwe, I. Balteanu, Z. Sun, O. P. Balaj, V. E. Bondybey, and M. K. Beyer, *Int. J. Mass Spectrom.* 254 (2006) 183–188.

[27] C.-K. Siu, S. J. Reitmeier, I. Balteanu, V. E. Bondybey, and M. K. Beyer, *Eur. Phys. J. D* 43 (2007) 189–192.

[28] L. Xiao and L. Wang, *J. Phys. Chem. A* 108 (2004) 8605–8614.

[29] K. Bhattacharyya and C. Majumder, *Chem. Phys. Lett.* 446 (2007) 374–379.

[30] M. Huda and L. Kleinman, *Phys. Rev. B* 74 (2006) 1–7.

[31] A. Fortunelli, *J. Mol. Struct.* 493 (1999) 233–240.

[32] A. Hellman and H. Grönbeck, *J. Phys. Chem. C* 113 (2009) 3674–3682.

[33] J. Rubio, S. Zurita, J. C. Barthelat, and F. Illas, *Chem. Phys. Lett.* 217 (1994) 283–287.

[34] M. Huda, M. Niranjan, B. Sahu, and L. Kleinman, *Phys. Rev. A* 73 (2006) 1–5.

[35] T. Li and P. B. Balbuena, *J. Phys. Chem. B* 105 (2001) 9943–9952.

[36] D. Dai and K. Balasubramanian, *J. Chem. Phys.* 103 (1995) 648-655.

[37] C. Zhou, J. Wu, T. J. D. Kumar, N. Balakrishnan, R. C. Forrey, and H. Cheng, *J. Phys. Chem. C* 111 (2007) 13786–13793.

[38] G. Kresse and J. Furthmiiller, *Comput. Mater. Sci.* 6 (1996) 15–50.

[39] G. Kresse and J. Hafner, *Phys. Rev. B* 47 (1993) 558–561.

[40] H. Pinto, R. Nieminen, and S. Elliott, *Phys. Rev. B* 70 (2004) 125402.

[41] P. Alemany, R. S. Boorse, J. M. Burlitch, and R. Hoffmann, *J. Phys. Chem.* 97 (1993) 8464–8475.

[42] T. R. Ward, P. Alemany, and R. Hoffmann, *J. Phys. Chem.* 97 (1993) 7691–7699.

[43] V. Cooper, A. Kolpak, Y. Yourdshahyan, and A. Rappe, *Phys. Rev. B* 72 (2005) 081409.

[44] A. Endou, R. Yamauchi, M. Kubo, A. Stirling, and A. Miyarnoto, *Appl. Surf. Sci*. 119 (1997) 318–320.

[45] Q. Ge and M. Neurock, *J. Am. Chem. Soc.* 126 (2004) 1551–1559.

[46] T. Q. Nguyen, M. C. S. Escaño, R. Tanaka, H. Nakanishi, and H. Kasai, *J. Phys. Soc. Japan* 78 (2009) 014706.

[47] K. Yamamoto, T. Imaoka, W.-J. Chun, O. Enoki, H. Katoh, M. Takenaga, and A. Sonoi, *Nat. Chem.* 1 (2009) 397–402.

[48] J. H. Kang, L. D. Menard, R. G. Nuzzo, and A. I. Frenkel, *J. Am. Chem. Soc.* 128 (2006) 12068–12069.

[49] F. Oemry, M. C. Escano, H. Kishi, S. Kunikata, H. Nakanishi, H. Kasai, H. Maekawa, K. Osumi, and Y. Tashiro, *J. Nanosci. Nanotechnol.* 11 (2011) 2844–2850.

[50] M. Andersson and A. Rosén, *J. Chem. Phys.* 117 (2002) 7051-7054.

[51] P. J. Feibelman, *Phys. Rev. B* 56 (1997) 2175–2182.

[52] A. D. Becke and K. E. Edgecombe, *J. Chem. Phys.* 92 (1990) 5397-5403.

[53] J. Perdew, K. Burke, and M. Ernzerhof, *Phys. Rev. Lett.* 77 (1996) 3865–3868.

[54] G. Kresse and J. Hafner, *Phys. Rev. B* 49 (1994) 251–269.

[55] G. Kresse, *Comput. Mater. Sci.* 6 (1996) 15–50.

[57] T. B. Terriberry, D. F. Cox, and D. A. Bowman, *Comput. Chem.* 26 (2002) 313–319.

[58] G. Henkelman, B. P. Uberuaga, and H. Jónsson, *J. Chem. Phys.* 113 (2000) 9901-9904.

[59] G. Henkelman and H. Jónsson, *J. Chem. Phys.* 113 (2000) 9978-9985.

[60] P. Gambardella, Ž. Šljivančanin, B. Hammer, M. Blanc, K. Kuhnke, and K. Kern, *Phys. Rev. Lett.* 87 (2001) 1–4.

[61] B. Stipe, M. Rezaei, W. Ho, S. Gao, M. Persson, and B. Lundqvist, *Phys. Rev. Lett.* 78 (1997) 4410–4413.

[62] Y. Dok Kim and G. Ganteför, *Chem. Phys. Lett.* 383 (2004) 80–83.

[63] A. Silvi, B, Savin, *Nature* 371 (1994) 683–686.

[64] T. Gomez, E. Florez, A. Rodriguez, and F. Illas, *J. Phys. Chem. C* 115 (2011) 11666–11672.

[65] J. Kua and W. A. Goddard, *J. Phys. Chem. B* 102 (1998) 9481–9491.

[66] R. B. Getman and W. F. Schneider, *ChemCatChem* 2 (2010) 1450–1460.

[67] B. Shan, N. Kapur, J. Hyun, L. Wang, J. B. Nicholas, and K. Cho, *J. Phys. Chem. C* 113 (2009) 710–715.

[68] A. Eichler and J. Hafner, *Phys. Rev. Lett.* 79 (1997) 4481–4484.

[69] S. Yotsuhashi, Y. Yamada, W. Diño, H. Nakanishi, and H. Kasai, *Phys. Rev. B* 72 (2005) 1–4.

[70] A. Eichler, F. Mittendorfer, and J. Hafner, *Phys. Rev. B* 62 (2000) 4744–4755.

[71] R. Avery, *Chem. Phys. Lett.* 96 (1983) 371–373.

[72] M. Bauer, C. Lei, K. Read, R. Tobey, J. Gland, M. Murnane, and H. Kapteyn, *Phys. Rev. Lett.* 87 (2001) 1–4.

[73] J. L. Gland, B. A. Sexton, and G. B. Fisher, *Surf. Sci.* 95 (1980) 587–602.

[74] E. Lewars, *Computational Chemistry: Introduction to The Theory and Applications of Molecular and Quantum Mechanics*. Boston, MA: Kluwer Academic, 2003, p. 32.

[75] R. P. Feynman, *Phys. Rev. B* 56 (1939) 340–343.

[76] P. Nordlander and M. Ronay, *Phys. Rev. B* 36 (1987) 4982–4989.

[77] M. Moldovan, M. A. Palacios, M. M. Gómez, G. Morrison, S. Rauch, C. McLeod, R. Ma, S. Caroli, A. Alimonti, F. Petrucci, B. Bocca, P. Schramel, M. Zischka, C. Pettersson, U. Wass, M. Luna, J. C. Saenz, and J. Santamaría, *Sci. Total Environ.* 296 (2002) 199–208.

[78] C. Mager-Maury, G. Bonnard, C. Chizallet, P. Sautet, and P. Raybaud, *ChemCatChem* 3 (2011) 200–207.

[79] F. C. Galisteo, R. Mariscal, M. L. Granados, M. D. Z. Poves, J. L. G. Fierro, V. Kroger, and R. L. Keiski, *Appl. Catal. B Environ.* 72 (2007) 272–281.

[80] H. Shinjoh, *Catal. Surv. from Asia* 13 (2009) 184–190.

[81] G. Wang, H. Wu, D. Wexler, H. Liu, and O. Savadogo, *J. Alloys Compd.* 503 (2010) L1–L4.

[82] Y. Chen, F. Yang, Y. Dai, W. Wang, and S. Chen, *J. Phys. Chem. C* 112 (2008) 1645–1649.

[83] J. Snyder, T. Fujita, M. W. Chen, and J. Erlebacher, *Nat. Mater.* 9 (2010) 904–907.

[84] B. M. Weiss and E. Iglesia, *J. Phys. Chem. C* 113 (2009) 13331–13340.

[85] B. Han, C. Miranda, and G. Ceder, *Phys. Rev. B* 77 (2008) 075410.

[86] J. Kitchin, J. Nørskov, M. Barteau, and J. Chen, *Phys. Rev. Lett.* 93 (2004) 4–7.

[87] P. G. Allen, S. D. Conradson, M. S. Wilson, S. Gottesfel, I. . D. Raistrick, J. Valerio, and M. Lovato, *J. Electroanal. Chem.* 384 (1995) 99–103.

[88] H. Imai, K. Izumi, M. Matsumoto, Y. Kubo, K. Kato, and Y. Imai, *J. Am. Chem. Soc.* 131 (2009) 6293–6300.

[89] O. S. Alexeev, S. Y. Chin, M. H. Engelhard, L. Ortiz-Soto, and M. D. Amiridis, *J. Phys. Chem. B* 109 (2005) 23430–23443.

[90] S. Mostafa, F. Behafarid, J. R. Croy, L. K. Ono, L. Li, J. C. Yang, A. I. Frenkel, and B. R. Cuenya, *J. Am. Chem. Soc.* 132 (2010) 15714–15719.

[91] S. Chen, J. P. K. Doyea, and D. J. Wales, *New J. Chem.* 733–744, 1998.

[92] L.-L. Wang and D. D. Johnson, *J. Am. Chem. Soc.* 131 (2009) 14023–14029.

[93] J. Wu, L. Qi, H. You, A. Gross, J. Li, and H. Yang, *J. Am. Chem. Soc.* 134 (2012) 11880–11883.

[94] D. Karhánek, T. Bučko, and J. Hafner, *J. Phys. Condens. Matter*. 22 (2010) 265006.

[95] S. K. Nayak, S. N. Khanna, B. K. Rao, and P. Jena, *J. Phys. Chem. A* 101 (1997) 1072–1080.

[96] S. Mukerjee, S. Srinivasan, M. P. Soriaga, and J. McBreen, *J. Phys. Chem.* 99 (1995) 4577–4589.

[97] M. Teliska, V. S. Murthi, S. Mukerjee, and D. E. Ramaker, *J. Electrochem. Soc.* 152 (2005) A2159-A2169.

[98] C. Lu and G. Henkelman, Phys. Chem. Lett. 2 (2011) 1237–1240.

[99] P. Gambardella, Ž. Šljivančanin, B. Hammer, M. Blanc, K. Kuhnke, and K. Kern, *Phys. Rev. Lett.* 87 (2001) 1–4.

[100] Z. Gu, P. B. Balbuena, *J. Phys. Chem. C* 111 (2007) 9877–9883.

[101] J. M. Bray, W. F. Schneider, *Langmuir* 27 (2011) 8177–8186.

[102] M. R. McClellan, F. R. Mcfeely, *Surf. Sci.* 123 (1983) 188–208.

[103] T. Jacob, B. V. Merinov, and W. A. Goddard, *Chem. Phys. Lett.* 385 (2004) 374–377.

[104] H. Wang, R. G. Tobin, D. K. Lambert, C. L. DiMaggio, and G. B. Fisher, *Surf. Sci.* 372 (1997) 267–278.

[105] F. Oemry, A. A. B. Padama, H. Kishi, S. Kunikata, H. Nakanishi, H. Kasai, H. Maekawa, K. Osumi, and K. Sato, *Jpn. J. Appl. Phys.* 51 (2012) 035002.

[106] G. A. Somorjai, *Langmuir* 7 (1991) 3176–3182.

[107] G. A. Somorjai, *Surf. Sci.* 242 (1991) 481–488.

[108] M. A. Van Hove and G. A. Somorjai, *Surf. Sci.* 299/300 (1994) 487–501.

[109] P. Rzeszotarski and Z. Kaszkur, *Phys. Chem. Chem. Phys.* 11 (2009) 5416–5421.

[110] B. Roldan Cuenya, J. R. Croy, S. Mostafa, F. Behafarid, L. Li, Z. Zhang, J. C. Yang, Q. Wang, and A. I. Frenkel, *J. Am. Chem. Soc.* 132 (2010) 8747–8756.

[111] A. Yevick and A. I. Frenkel, "Effects of surface disorder on EXAFS modeling of metallic clusters," *Phys. Rev. B*, vol. 81, no. 11, p. 115451, Mar. 2010.

[112] Y. Nagai, T. Hirabayashi, K. Dohmae, N. Takagi, T. Minami, H. Shinjoh, and S. Matsumoto, *J. Catal.* 242 (2006) 103–109.

[113] D. H. Parker, M. E. Bartram, and B. E. Koel, *Surf. Sci.* 217 (1989) 489–510.

[114] A. Jentys, *Phys. Chem. Chem. Phys.* 1 (1999) 4059–4063.

[115] C. Hock, S. Straßburg, H. Haberland, B. V. Issendorff, A. Aguado, M. Schmidt, *Phys. Rev. Lett.* 101 (2008) 023401.

[116] G. Henkelman, A. Arnaldsson, H. Jónsson, *Comput. Mater. Sci.* 36 (2006) 354–360.

[117] R. F. W. Bader, *Atoms in Molecules: A Quantum Theory*. Oxford: Oxford University Press, 1990.

[118] N. Seriani, Z. Jin, W. Pompe, L. Ciacchi, *Phys. Rev. B* 76 (2007) 155421.

[119] C.-B. Wang, C.-T. Yeh, *J. Catal.* 178 (1998) 450–456.

[120] J. R. Croy, S. Mostafa, L. Hickman, H. Heinrich, B. R. Cuenya, *Appl. Catal. A* 350 (2008) 207–216.

[121] P. Feibelman, *Phys. Rev.* B 56 (1997) 10532–10537.

Appendices

A. Introduction to Density Functional Theory

A.1 Schrödinger equation with Born-Oppenheimer approximation

Let us first consider the time-independent, non-relativistic Schrödinger equation as written below

$$\hat{H}\Psi_i(\vec{r}_1, \vec{r}_2, \vec{r}_3, \ldots, \vec{r}_N, \vec{R}_1, \vec{R}_2, \vec{R}_3, \ldots, \vec{R}_M) = E_i\Psi_i(\vec{r}_1, \vec{r}_2, \vec{r}_3, \ldots, \vec{r}_N, \vec{R}_1, \vec{R}_2, \vec{R}_3, \ldots, \vec{R}_M) \quad (2\text{-}1)$$

$\hat{H}$ is the Hamiltonian for a system consisting of M nuclei and N electrons where its expansion is

$$\hat{H} = -\sum_i^N \frac{1}{2}\nabla_i^2 - \sum_A^N \frac{1}{M_A}\frac{1}{2}\nabla_A^2 - \sum_A^M \sum_i^N \frac{Z_A}{r_{iA}} + \sum_{i<j}^N \sum_j^N \frac{1}{r_{ij}} + \sum_{B<A}^M \sum_A^M \frac{Z_A Z_B}{R_{AB}} \quad (2\text{-}2)$$

Here, A and B refer to the M nuclei while i and j denote the N electrons in the system. The first two terms describe the kinetic energy of the electrons and nuclei. The last three terms represent the attractive electrostatic nuclei-electron interactions ($\hat{V}_{Ne}$), repulsive potential due to the electron-electron ($\hat{V}_{ee}$) and nucleus-nucleus interactions ($\hat{V}_{NN}$), respectively. Born-Oppenheimer approximation, a concept that assumes the nuclei move much slower than the electrons due to the nuclei's massive mass, further imposes that the nuclear kinetic energy is zero and their potential energy is merely a constant. As the result, the previous Hamiltonian operator can be reduced and only the electronic Hamiltonian ($\hat{H}_{elec}$) in concert with $\hat{V}_{NN}$ that is being evaluated

$$\hat{H}_{elec} = -\sum_i^N \frac{1}{2}\nabla_i^2 - \sum_A^M \sum_i^N \frac{Z_A}{r_{iA}} + \sum_{i<j}^N \sum_j^N \frac{1}{r_{ij}} = \hat{T} + \hat{V}_{Ne} + \hat{V}_{ee} \quad (2\text{-}3)$$

The solution of the Schrödinger equation above is the electronic wave function Ψ_{elec} and the electronic energy E_{elec}. The total energy E_{tot} is then the sum of E_{elec} and the constant nuclear repulsion term E_{nuc}. The equation (2-3) would be later adopted by Hohenberg-Kohn

theorem to demonstrate that the electron density uniquely determines the (electronic) Hamiltonian operator particularly the external potential V_{ext} which refers to $\hat{V}_{Ne}$.

A.2 The Thomas-Fermi model

The central quantity in DFT is the electron density which defined as the integral over the spin coordinates of all electrons within spatial space of variable $\vec{r}$

$$\rho(\vec{r}) = N \int \dots \int |\Psi(\vec{r}_1, \vec{r}_2, \dots, \vec{r}_N)|^2 d\vec{r}_1 d\vec{r}_2 \dots d\vec{r}_N \quad (2\text{-}4)$$

$\rho(\vec{r})$ determines the probability of finding any of the N electrons within volume element $d\vec{r}$. In 1927, the first DFT model was proposed by Thomas and Fermi. The model is based on the uniform electron gas approach and the energy of the system according to Thomas-Fermi (TF) model is calculated using the following equation

$$E_{TF}[\rho(\vec{r})] = \frac{3}{10}(3\pi^2)^{2/3} \int \rho^{\frac{5}{3}}(\vec{r})\, d\vec{r} - Z \int \frac{\rho(\vec{r})}{r} d\vec{r} + \frac{1}{2} \int \int \frac{\rho(\vec{r}_1)\rho(\vec{r}_2)}{r_{12}} d\vec{r}_1 d\vec{r}_2 \quad (2\text{-}5)$$

The first term in is the functional for the TF kinetic energy, while the second and third terms are corresponding to the classical expression for attractive nuclear-electron and repulsive electron-electron interactions, respectively. In order to get the true ground-state energy E_0, Thomas and Fermi employed variational principle where the energy in the equation above is minimized under the constraint of N, the number of electrons. However, at that the time their idea was hardly acceptable although it was seem reasonable. It was not until 1964, when Hohenberg and Kohn put legitimate theorem that supports the idea of E as a functional of $\rho(\vec{r})$.

A.3 Hohenberg-Kohn theorem

The first Hohenberg-Kohn (HK) theorem states that the external potential $V_{ext}(\vec{r})$ is a unique functional of $\rho(\vec{r})$ since $V_{ext}(\vec{r})$ fixes $\hat{H}$ and therefore the full many particle ground state is a unique potential of $\rho(\vec{r})$. As a proof, let us assume two external potential $V_{ext}(\vec{r})$ and $V'_{ext}(\vec{r})$ which differ by a constant, and each giving the same $\rho(\vec{r})$ for its ground state,

we would have two Hamiltonians $\hat{H}$ and $\hat{H}'$ whose ground-state densities are the same although the normalized wave functions Ψ and Ψ' would be different. Taking Ψ' as a trial wave function for $\hat{H}$ problem

$$E_0 < \langle\Psi'|\hat{H}|\Psi'\rangle = \langle\Psi'|\hat{H}'|\Psi'\rangle + \langle\Psi'|\hat{H} - \hat{H}'|\Psi'\rangle = E_0' + \int \rho(\vec{r})[V_{ext}(\vec{r}) - V_{ext}'(\vec{r})]\mathrm{d}\vec{r} \tag{2-6}$$

where E_0 and E_0' are the ground-state energies for $\hat{H}$ and $\hat{H}'$, respectively. In similar way, taking Ψ as a trial wave function for $\hat{H}'$ problem

$$E_0' < \langle\Psi|\hat{H}'|\Psi\rangle = \langle\Psi|\hat{H}|\Psi\rangle + \langle\Psi|\hat{H}' - \hat{H}|\Psi\rangle = E_0 + \int \rho(\vec{r})[V_{ext}'(\vec{r}) - V_{ext}(\vec{r})]\mathrm{d}\vec{r} \tag{2-7}$$

Adding eq. (2-6) and (2-7), we would obtain $E_0 + E_0' < E_0' + E_0$, a contradiction. Hence, two different $V_{\mathrm{ext}}(\vec{r})$ and $V_{ext}'(\vec{r})$ cannot give the same $\rho(\vec{r})$ for their ground state. In conclusion, $\rho(\vec{r})$ through N and $V_{\mathrm{ext}}(\vec{r})$ determines ground-state Hamiltonian $\hat{H}$ including the total energy $E[\rho]$. The total energy now can be written as

$$E[\rho] = E_{\mathrm{Ne}}[\rho] + \mathrm{T}[\rho] + E_{\mathrm{ee}}[\rho] = \int \rho(\vec{r})V_{Ne}(\vec{r})d\vec{r} + \mathrm{F_{HK}}[\rho] \tag{2-8}$$

where

$$\mathrm{F_{HK}}[\rho] = \mathrm{T}[\rho] + E_{\mathrm{ee}}[\rho] \tag{2-9}$$

and

$$E_{\mathrm{ee}}[\rho] = \frac{1}{2}\int\int \frac{\rho(\vec{r}_1)\rho(\vec{r}_2)}{r_{12}} d\vec{r}_1 d\vec{r}_2 + E_{\mathrm{ncl}} = J[\rho] + E_{\mathrm{ncl}}[\rho] \tag{2-10}$$

$J[\rho]$ is classical repulsive electron-electron interactions, while E_{ncl} is the non-classical contribution to $J[\rho]$, self-interaction correction, exchange, and Coulomb correlation. Finally, the second HK theorem states that $\mathrm{F_{HK}}[\rho]$, the functional that delivers the ground state energy of the system, delivers the lowest energy if and only if the input density is the true ground state density ρ_0. This condition could be achieved by implementing the variational principle:

$$E_0 \leq \mathrm{E}[\tilde{\rho}] = \mathrm{T}[\tilde{\rho}] + E_{\mathrm{Ne}}[\tilde{\rho}] + E_{\mathrm{ee}}[\tilde{\rho}] \tag{2-11}$$

where $\tilde{\rho}$ is any trial electron density. The major challenge that left in HK theorem is how to get explicit form of the functionals T[ρ] and E_{ncl}[ρ].

A.4 Kohn-Sham equation

In order to solve the problem of HK theorem above, Kohn and sham proposed a (fictitious) non-interacting of kinetic energy which has the same electron density as the real interacting one

$$T_S = -\frac{1}{2}\sum_i^N \langle \Psi_i | \nabla^2 | \Psi_i \rangle \qquad \rho_S(\vec{r}) = \sum_i^N \sum_s |\Psi_i(\vec{r}, s)|^2 = \rho(\vec{r}) \tag{2-12}$$

where Ψ_i are the orbitals of the non-interacting system. Of course, T_S is not equal to the true kinetic energy of the system. The Hohenberg-Kohn functional F_{HK}[ρ] can be rewritten as

$$F_{HK}[\rho] = T_S[\rho] + J[\rho] + E_{XC}[\rho] \tag{2-13}$$

where E_{XC} is defined by comparing equations (2-9) and (2-13) which yields

$$E_{XC}[\rho] \equiv (T[\rho] - T_S[\rho]) + (E_{ee}[\rho] - J[\rho]) \tag{2-14}$$

The exchange and correlation energy E_{XC} is the functional that contains everything that is unknown. In the next sub-section, the approximation method that commonly used in DFT to acquire the value of E_{XC} will be further elucidated. By inserting eq. (2-13) into eq. (2-8), the expression for the energy of the interacting system

$$\begin{gathered} E[\rho] = T_S[\rho] + J[\rho] + E_{XC}[\rho] + E_{Ne}[\rho] = \\ -\frac{1}{2}\sum_i^N \langle \Psi_i | \nabla^2 | \Psi_i \rangle + \frac{1}{2}\sum_i^N \sum_j^N \int \int |\Psi_i(\vec{r}_1)|^2 \frac{1}{r_{12}^2} \left|\Psi_j(\vec{r}_2)\right|^2 d\vec{r}_1\, d\vec{r}_2 + E_{XC}[\rho] \\ -\sum_i^N \sum_A^M \int \frac{Z_A}{r_{iA}} |\Psi_i(\vec{r})|^2 \, d\vec{r}_i \end{gathered} \tag{2-15}$$

If the variational principle is applied, particular condition of the orbitals Ψ_i must be fulfilled in order to minimize the energy expression above under the constraint $\langle \Psi_i | \Psi_j \rangle = \delta_{ij}$. That condition is satisfied when the Hamiltonian of that E[ρ] in eq. (2-15) can be resolved. The Hamiltonian that we are looking for is manifested in Kohn-Sham equation

$$(-\frac{1}{2}\nabla^2 + [\int \frac{\rho(\vec{r}_2)}{r_{12}} + V_{XC}(\vec{r}_1) - \sum_A^M \frac{Z_A}{r_{1A}}])\,\Psi_i = (-\frac{1}{2}\nabla^2 + V_{eff}(\vec{r}_1))\Psi_i = \epsilon_i \Psi_i \qquad (2\text{-}16)$$

the exchange-correlation potential V_{XC} is defined as the functional derivative of E_{XC} with respect to ρ ($V_{XC} = \delta E_{XC}/\delta\rho$). The important thing is that if the exact forms of E_{XC} and V_{XC} are known, the Kohn-Sham equation would yield the exact energy of the system.

A.5 Local density approximation (LDA) and generalized gradient approximation (GGA)

The exchange-correlaction energy E_{XC} cannot be analytically calculated, the energy can only be obtained through self-consistent numerical calculation. For that reason, a method to approximate the value of E_{XC} should be developed and applied in the DFT computational techniques. The earliest exchange-correlaction functional approximation is probably local density approximation (LDA) which basically based on the uniform electron gas model.

$$E_{XC}^{LDA}[\rho] = \int \rho(\vec{r})\epsilon_{XC}(\rho(\vec{r}))d\vec{r} \qquad (2\text{-}17)$$

Here, $\epsilon_{XC}(\rho(\vec{r}))$ is the exchange-correlation energy per particle of an uniform electron gas of density $\rho(\vec{r})$. This energy per particle is weighted with the probability $\rho(\vec{r})$ that there is an electron at certain position. The common weakness that attribute to LDA approach is its moderate accuracy that considered being insufficient for most applications in chemistry and it fails in systems that dealing with heavy fermions. To overcome this problem, a more accurate generalized gradient approximation (GGA) was invented. GGA added the density information about the gradient of the charge density, $\nabla\rho(\vec{r})$ in order to account for the non-

homogeneity of the true electron density. The expression for GGA exchange-correlation energy is

$$E_{XC}^{GGA}[\rho_\alpha, \rho_\beta] = \int f(\rho_\alpha, \rho_\beta, \nabla\rho_\alpha, \nabla\rho_\beta)\, \mathrm{d}\vec{r} \tag{2-18}$$

GGA approximation has been able to reduce the LDA errors of atomization energies of standard set of small molecules by a factor 3-5. This improved accuracy has made DFT a significant component of quantum chemistry.

B. Climbing-image nudged elastic band (Ci-NEB)

Nudged elastic band (NEB) is a method to find a minimum energy path (MEP) between a pair of stable states, initial and final states, where those states are local minima on the potential energy surface (PES). NEB calculation uses a string of images (geometric configurations of the system) to describe a reaction pathway. The images along the NEB are relaxed to the MEP through a force projection scheme in which potential forces act perpendicular to the band, and spring forces act along the band. To make these projections, the tangent along the path $\hat{\tau}$ is defined as the unit vector to the higher energy neighboring image as can be seen in Figure 2.1.

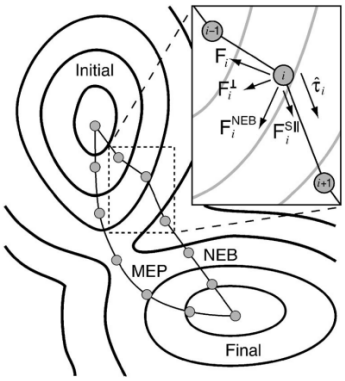

Figure 2.1 Two components make up the nudged elastic band for $\mathbf{F}^{\mathrm{NEB}}$: the spring force $\mathbf{F}_{\mathrm{i}}^{\mathrm{S}\parallel}$, along the tangent $\hat{\tau}_i$, and the perpendicular force due to the potential $\mathbf{F}_{\mathrm{i}}^{\perp}$. The unprojected force do to the potential $\mathbf{F}_{\mathrm{i}}$ is also shown for completeness.

The NEB force on image in *i* contains two independent components

$$\mathbf{F}_i^{\mathrm{NEB}} = \mathbf{F}_i^{\perp} + \mathbf{F}_i^{\mathrm{S}\parallel} \tag{2-19}$$

where $\mathbf{F}_i^{\perp}$ is the component of the force due to the potential perpendicular to the band

$$\mathbf{F}_i^{\perp} = -\nabla E(\mathbf{R}_i) + \nabla E(\mathbf{R}_i) \cdot \hat{\tau}_i \hat{\tau}_i \tag{2-20}$$

and $\mathbf{F}_i^{\mathrm{S}\parallel}$ is the spring force parallel to the band

$$\mathbf{F}_i^{\mathrm{S}\parallel} = k(|\mathbf{R}_{i+1} - \mathbf{R}_i| - |\mathbf{R}_i - \mathbf{R}_{i-1}|)\,\hat{\tau}_i \tag{2-21}$$

$\mathbf{R}_i$ is the position of the *i*th image and k is the spring constant. Climbing-image nudged elastic band (Ci-NEB) method that introduced by Henkelmann and coworkers [58] makes a small modification to the NEB method. This new method maintains the shape of the MEP but rigorous convergence to a saddle point is also obtained without adding any significant computational effort. After a few iterations with the regular NEB, the image with the highest energy $i_{\max}$ is identified. The force on this one image is not given by Eq. (2-20) but rather by

$$\mathbf{F}_{i_{\max}} = -\nabla E(\mathbf{R}_{i_{\max}}) + 2\nabla E(\mathbf{R}_{i_{\max}}) \cdot \hat{\tau}_{i_{\max}} \hat{\tau}_{i_{\max}} \tag{2-22}$$

Based on the equation above, the maximum energy image is not affected by the spring force at all. Therefore, the spacing of the images will be different on each side of the climbing image. As the image moves up to the saddle point, image on one side will get compressed and on the other side spread out. The only issue is to have enough image close to the climbing image(s) to get a good estimate of the reaction coordinate, since this determines the climbing direction.

Acknowledgement

First, I would like to sincerely thank my supervisor, Prof. Hideaki Kasai for his guidance and endless assistance helped me throughout my stay here in Japan and whose advice, direction and endless source of knowledge in the subject of my thesis. I could not have done all of these without his help. I gratefully acknowledge Prof. Hiroshi Nakanishi and Prof. Wilson Agerico Dino for many insightful discussions, constructive comments and suggestions regarding my work that helped me towards its completion.

My humble gratitude also to the panelists of my thesis, Prof. Yoji Shibutani, Prof. Toshiaki Munakata and Prof. Kazunori Sato, for their valuable discussions and suggestions towards the improvement of this thesis from both theoretical and experimental perspectives.

I thank also all the staff members of Kasai Laboratory, Ms. Reiko Tanaka, Ms. Mayuko Aihara, Ms. Keiko Furuyama, Dr. Mamoru Sakaue, Ms. Ikuko Nojiri, Ms. Hizuru Ito and Ms. Sayoko Sakai, for all their assistance and support, especially in the translation of many documents for me and the scholarship information that you provided. To all former and current students and postdoc members of Kasai Laboratory, thank you for your warm friendship during my stay in Japan. Particularly, former students of Kasai Laboratory, Dr. Handoko Setyo Kuncoro, Dr. Mary Clare Sison Escano, and Dr. Abdulla Sarhan for their companionship and happy moments together. To the members of ISUZU group team, Dr. Hirofumi Kishi, Mr. Shinichi Kunikata, Dr. Tien Quang Nguyen, Mr. Kohei Oka, and Mr. Ryan L. Arevalo for the good years working together and being supportive in every possible way. Many thanks to all my friends in Indonesian Student Association for their kind support and help. To all my foreigner and Japanese friends out there, thank you so much for all the experience, joy, and camaraderie that we had shared in the past, it has been a great pleasure to know you all guys.

Finally, to my family and my little brothers in Indonesia especially my parents who have been supportive in many possible ways during my study in Japan, I would like to say thank you for all your prayer and support.

List of Publications

1. F. Oemry, M. C. Escaño, H. Kishi, S. Kunikata, H. Nakanishi, H. Kasai, H. Maekawa, K. Osumi, and Y. Tashiro, "*Nitrogen Monoxide Adsorption on Pt_4 Clusters Coated on $\gamma Al_2O_3(111)$ Surface*", J. Nanosci. Nanotechnol. 11 (2011) 2844.

2. W. T. Cahyanto, F. Oemry, A. A. B. Padama, M. Sakaue, R. Belkada, S. M. Aspera, M. Chikaishi, S. Kunikata, H. Nakanishi, H. Kasai, H. Maekawa, K. Osumi, and Y. Tashiro, "*Favorable pathway of O_2 dissociative adsorption on a single platinum adatom coated on gamma-alumina (111) surface: a density functional theory study*", Jpn. J. Appl. Phys. 50 (2011) 105602.

3. F. Oemry, A. A. B. Padama, H. Kishi, S. Kunikata, H. Nakanishi, H. Kasai, H. Maekawa, K. Osumi, and K. Sato, "*Effects of Cluster Size on Platinum-Oxygen Bonds Formation in Small Platinum Clusters*", Jpn. J. Appl. Phys. 51 (2012) 035002.

4. H. Kishi, F. Oemry, T. Q. Nguyen, S. Kunikata, H. Nakanishi, H. Kasai, H. Maekawa, and K. Osumi, "*Study of NO Oxidation Reaction over the Pt Cluster Supported on $\gamma Al_2O_3(111)$ surface*", Curr. Appl. Phys. 12 (2012) S110-S114.

5. F. Oemry, H. Nakanishi, H. Kasai, H. Maekawa, K. Osumi, K. Sato, "*Adsorbed Oxygen-Induced Cluster Reconstruction on Core-shell Ni@Pt and Pt Clusters*", J. Alloys Comp. 594 (2014) 93-101.

6. F. Oemry, H. Nakanishi, H. Kasai, H. Maekawa, K. Osumi, K. Sato, "*Atomic Oxygen Adsorption on Core-Shell Ni@Pt and Pure Pt Nanoparticles*", submitted to Journal of the Vacuum Society of Japan (under review, 2014).

List of Conferences Attended

1. F. Oemry, M. C. Escaño, H. Kishi, S. Kunikata, H. Nakanishi, H. Kasai, H. Maekawa, K. Osumi, and Y. Tashiro, " *NO Adsorption on Pt_4 Tetramer Coated on gamma-Al_2O_3(111) Surface*", 5th Handai Nanoscience and Nanotechnology International Symposium, Osaka, Japan, 1-3 September 2009.

2. F. Oemry, M. C. Escaño, H. Kishi, S. Kunikata, H. Nakanishi, H. Kasai, H. Maekawa, K. Osumi, and Y. Tashiro, " *NO Adsorption on Pt_4 Tetramer Coated on gamma-Al_2O_3(111) Surface*", Second International Symposium on Atomically Controlled Fabrication Technology, Osaka, Japan, 25-26 November 2009.

3. F. Oemry, 坂上護, 岸浩史、国方伸一、中西寛、笠井秀明、前川弘吉、大角和生、田代欣久,"*担体効果の影響を受けた Pt 原子および Pt_4クラスタ上における O_2解離吸着特性*", 第 51 回真空に関する連合講演会, Osaka, Japan, 4-6 November 2011.

4. F. Oemry, H. Kishi, S. Kunikata, H. Nakanishi, H. Kasai," *Effects of Cluster Size on Pt-O Bonds Formation in Small Platinum Clusters*", 4th GCOE on Atomically Controlled Fabrication Technology, Osaka, Japan, 31 October – 2 November 2012.

5. F. Oemry, H. Kishi, S. Kunikata, H. Nakanishi, H. Kasai," *Effects of Cluster Size on Pt-O Bonds Formation in Small Platinum Clusters*", ECO-MATES 2011, Osaka, Japan, 28-30 November 2012.